Master's Thesis

석사 학위논문

Characterization of an advanced MEMS artificial basilar membrane using XeF_2 etching in the air and fluid

Hyejin Jeon (전 혜 진 全 惠 眞)

Department of

Robotics Engineering

DGIST

2016

Master's Thesis

석사 학위논문

Characterization of an advanced MEMS artificial basilar membrane using XeF$_2$ etching in the air and fluid

Hyejin Jeon (전 혜 진 全 惠 眞)

Department of

Robotics Engineering

DGIST

2016

Characterization of an advanced MEMS artificial basilar membrane using XeF$_2$ etching in the air and fluid

Advisor   :   Professor   Hongsoo Choi

Co-advisor :   Professor   Ji-Woong Choi

By

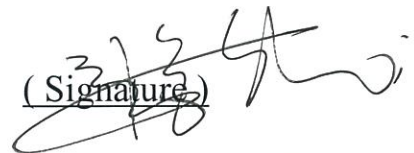Hyejin Jeon

Department of Robotics Engineering

DGIST

A thesis submitted to the faculty of DGIST in partial fulfillment of the requirements for the degree of Master of Science in the Department of Robotics Engineering. The study was conducted in accordance with Code of Research Ethics[1]

01. 08. 2016

Approved by

Professor   Hongsoo Choi   (Signature)
(Advisor)

Professor   Ji-Woong Choi   (Signature)
(Co-Advisor)

Characterization of an advanced MEMS artificial basilar

membrane using XeF_2 etching in the air and fluid

Hyejin Jeon

Accepted in partial fulfillment of the requirements for the degree
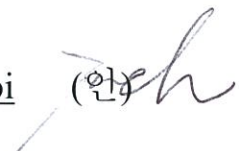
of Master of Science.

12. 03. 2015

Head of Committee   <u>Prof. Hongsoo Choi</u>

Committee Member   <u>Prof. Ji-Woong Choi</u>

Committee Member   <u>Prof. Jae-Eun Jang</u>

ABSTRACT

Cochlear implants (CIs) are implanted electronic devices for hearing recover of patients who have profoundly hearing loss caused by damaged hair cells in the cochlea. Although CIs have been conventionally successful, it has some limitations: necessity of extracorporeal devices, exposure of a disability by extracorporeal devices, requirement of large power, frequent recharging, and complicated signal processing circuits. To overcome these limitations, many researchers proposed the artificial basilar membranes (ABMs) to develop fully implantable CIs using microelectromechanical system (MEMS) technology. The ABM mimics the function of cochlea such as frequency selectivity and acoustic to electrical energy conversion. In the previous studies of our group, Kim et $al.$ developed an ABM consisting of an aluminum nitride (AlN) beam array with narrow supports. However, the piezoelectric voltage output was noise level because the narrow supports lead to a rigid body motion of beams. To increase the piezoelectric output of an ABM, Jang et $al.$ proposed an ABM fabricated by using a silicon-on-insulator (SOI) wafer and deep reactive ion etching (DRIE). Although the Jang et $al.$'s ABM showed the enhanced piezoelectric output performance, their fabrication process was too complicated with relatively high production cost.

In this paper, we fabricated an advanced MEMS ABM based on XeF_2 etching technology. The XeF_2 etching enable the total fabrication process to very simple with relatively low production costs in comparison with DRIE. Also, the low-pressure chemical

vapor deposition silicon nitride (LPCVD Si_3N_4) was used to reduce the lateral bending of beam which was caused by residual stress. In addition to fabrication process, the all beams of ABM were designed to continuous beam structure without narrow supports to avoid rigid body motion of beam.

The displacement and piezoelectric output of each beam were measured using a scanning laser-Doppler vibrometer (SLDV) for acoustic or electric stimulus. During acoustic stimulus, the fabricated ABM showed a frequency selectivity in the range 10.5 - 36.5 kHz and the piezoelectric voltage output in the range 2 - 5 µV. It also showed a frequency selectivity in the range 11.1 - 47.7 kHz for electric stimulus. Also, the frequency selectivity of the fabricated ABM was estimated in the fluid. Since the viscous-damping effect of water, the resonance frequency was shifted from 11.1 - 47.7 kHz in air to 3.1 - 11.9 kHz in fluid.

From these results, the fabricated ABM has the two functions of cochlea which are frequency selectivity and acoustic-to-electric energy conversion. Also, we identified the feasibility as substitute of the conventional CIs and the potential as fully implantable device

Keywords: artificial basilar membrane, AlN beam array, XeF_2 etching, MEMS, resonance frequency, Piezoelectric output voltage.

Contents

List of Figures

5

List of Tables

1. INTRODUCTION

1.1 Background

1.1.1 Human ear anatomy and cochlea mechanism

The human ear consists of three sections: the outer ear, middle ear, and inner ear, as shown in figure 1.1. The outer ear consists of the pinna and external auditory meatus. The pinna, which is made of the cartilage, gathers the sound using its physical shape. The gathered sound is delivered to the tympanic membrane using resonance effect of the external auditory meatus. The middle ear consists of the tympanic membrane and auditory ossicle. The tympanic membrane is a border between the outer ear and the middle ear. It plays an important role in spreading the sound. The tympanic membrane is vibrating like a drum caused by the sound coming in through the external auditory meatus. The vibration of the tympanic membrane is transferred to the auditory ossicle in middle ear [1]. The inner ear consists of the semi-circular canals, utricle, saccule, and cochlea. The utricle, saccule, and semi-circular canals are parts of the vestibular system. The core organization of the inner ear that is needed to recognize the sound is a cochlea in ear. The core organization of the inner ear that is needed to recognize the sound is a cochlea in ear. The vibration of the stapes, which is a part of auditory ossicle, is transferred to the basilar membrane from through the lymph fluid in cochlea. Whenever the lymph fluid is shaking in cochlea, the basilar membrane is vibrating [2]. The stereocilia opens ionic channel due to deflection and the potential difference to excite the cochlear nerve is created [3, 4]. The electrical signals are transmitted to the brain. As a results, the human ear perceives in the frequency range of 20Hz - 20 kHz and sound pressure as low as 20 μPa [5-8]
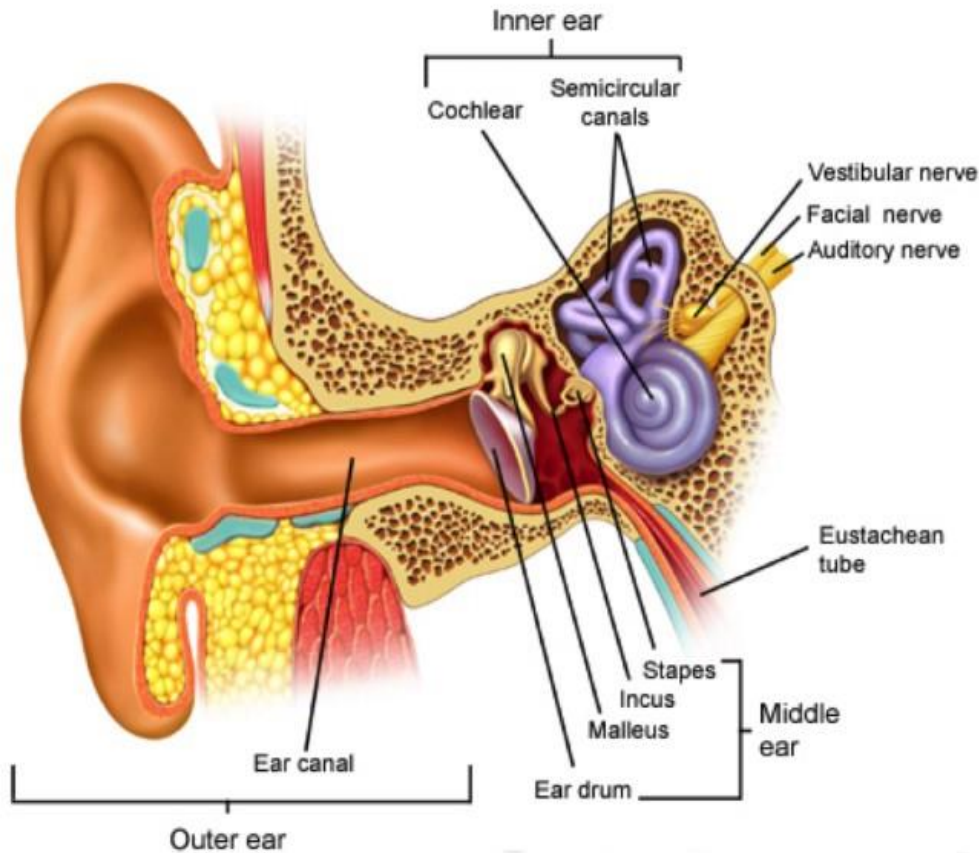
Figure 1.1 The human auditory system: the outer ear, middle ear, and inner ear.

In particular, the cochlea is an important organ for sound perception in human auditory system. A key component of the signal transduction occurs in the cochlea in the inner ear. The cochlea has two key functions which are the frequency selectivity of basilar membrane (BM) and the generation of electric signal in the OHC [7-9]. The cochlea consists of three liquid-filled chambers: the scala vestibule, scala media, and scala tympani. The BM is located between the scala media and the scala tympani that separates the two chambers [10, 11]. It provides the mechanical frequency selectivity of the cochlea. When the tympanic membrane is vibrating caused by the sound, the vibration of the stapes makes a hydraulic pressure difference between the scala vestibule and the scala tympani. The pressure difference between the two fluid-filled chambers creates a traveling wave along the BM, as shown in figure 1.2(a) [12-16].
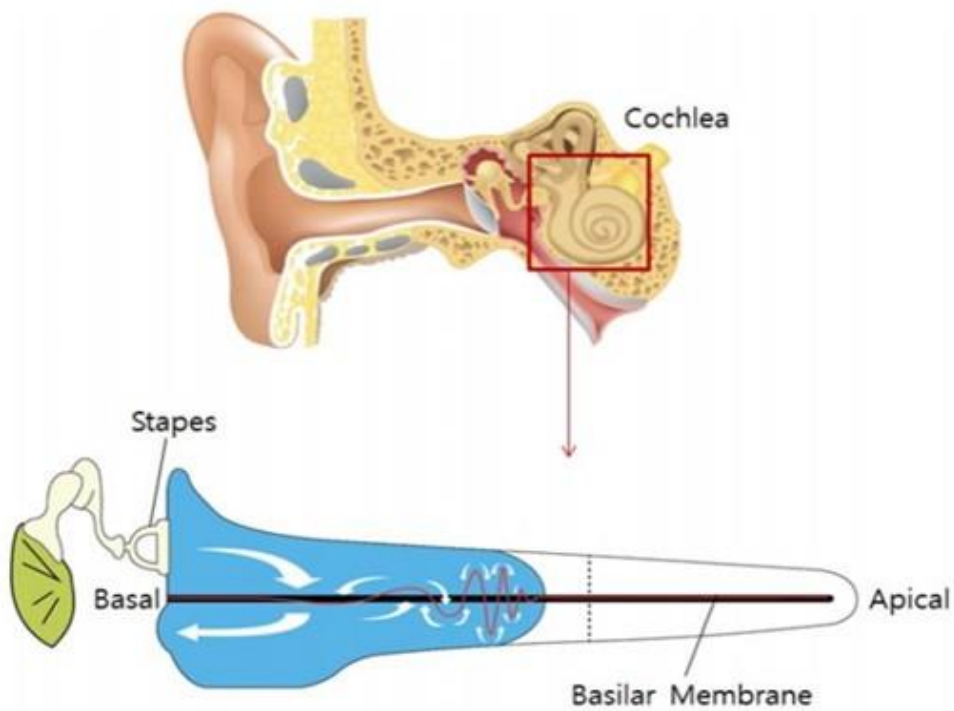
(a)
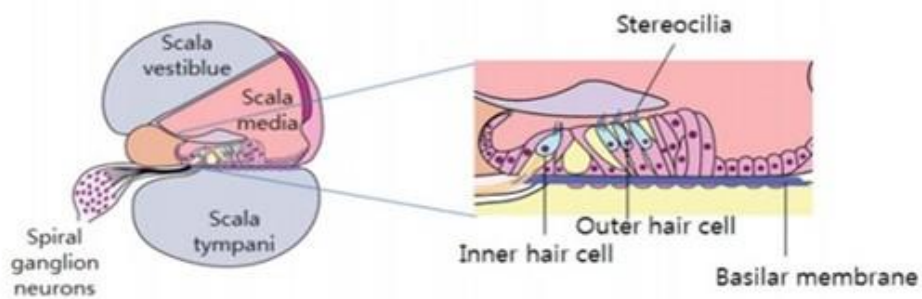
(b)

Figure 1.2 The function of a cochlea: (a) Passive frequency reaction of the basilar membrane (b) Anatomy of the cochlea and organ of Corti [6].

1.1.2 Cochlear implants

The sensorineural hearing loss is often caused by the damage on hair cells of cochlea, as shown in figure 1.3 (b). Figure 1.3 shows normal hair cells and damaged hair cells in figure 1.3 (a), (b). The hair cells convert acoustic sounds to electric signals that stimulate auditory nerves. If the hair cells are damaged, the electric signals are not generated in hair cells.
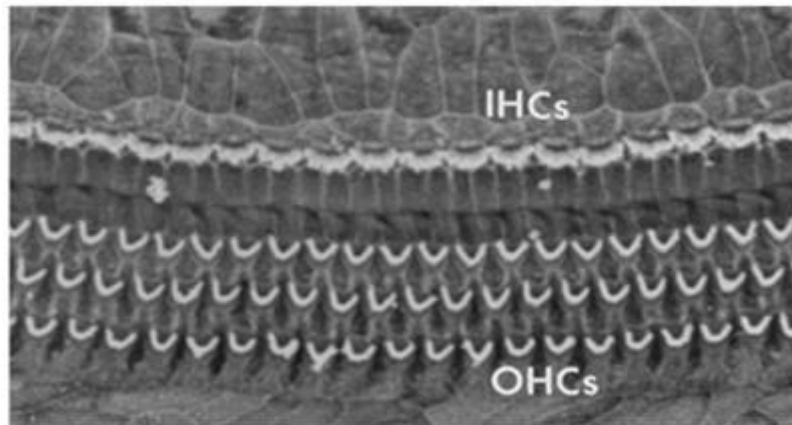
(a)
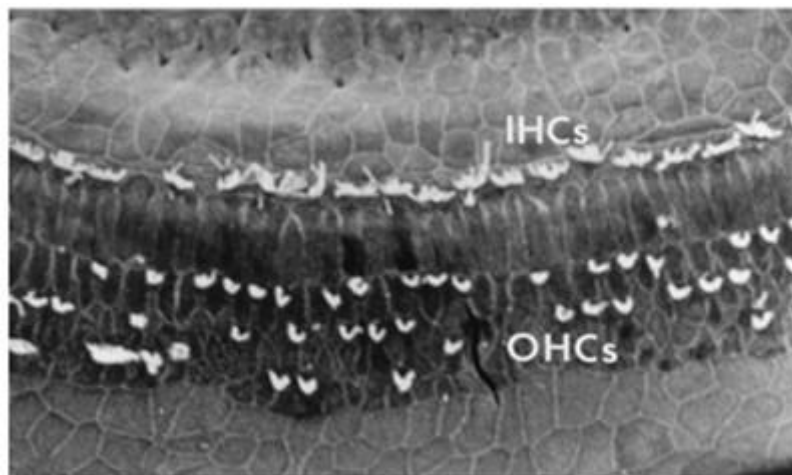
(b)

Figure 1.3 SEM image of hair cells in cochlea: (a) Normal hair cells (b) Damaged hair cells [17].

CI is a medical device for restoration of patients' hearing that is lost by damaged hair cells in the cochlea [18-20]. It is well used as a clinical treatment for the hearing loss in children and adults [21-23]. The current artificial cochlea has two parts, an internal part and external part. An internal part consists of an implantable electrode array for stimulation. An external part calls consists of a microphone, sound processor and battery. Figure 1.4 shows the parts of a cochlear implant in the human ear. First, a sound processor, which is worn behind the ear, transforms sound signals into a digital code. It has a battery that supplies the power to the entire system. Second, a digital code is transmitted by the coil of antenna on the outside of head to the internals. The antenna is attached in place via a magnet that is attracted to internal receiver. Third, a digital code is converted into electrical signals to stimulate auditory primary neuron. The electrical signals were transferred along the electrode array inserted in the cochlea. Fourth, these electrodes stimulate the auditory nerves, which then sends the electrical signals to the brain where they are interpreted as sound [1, 24, 25].
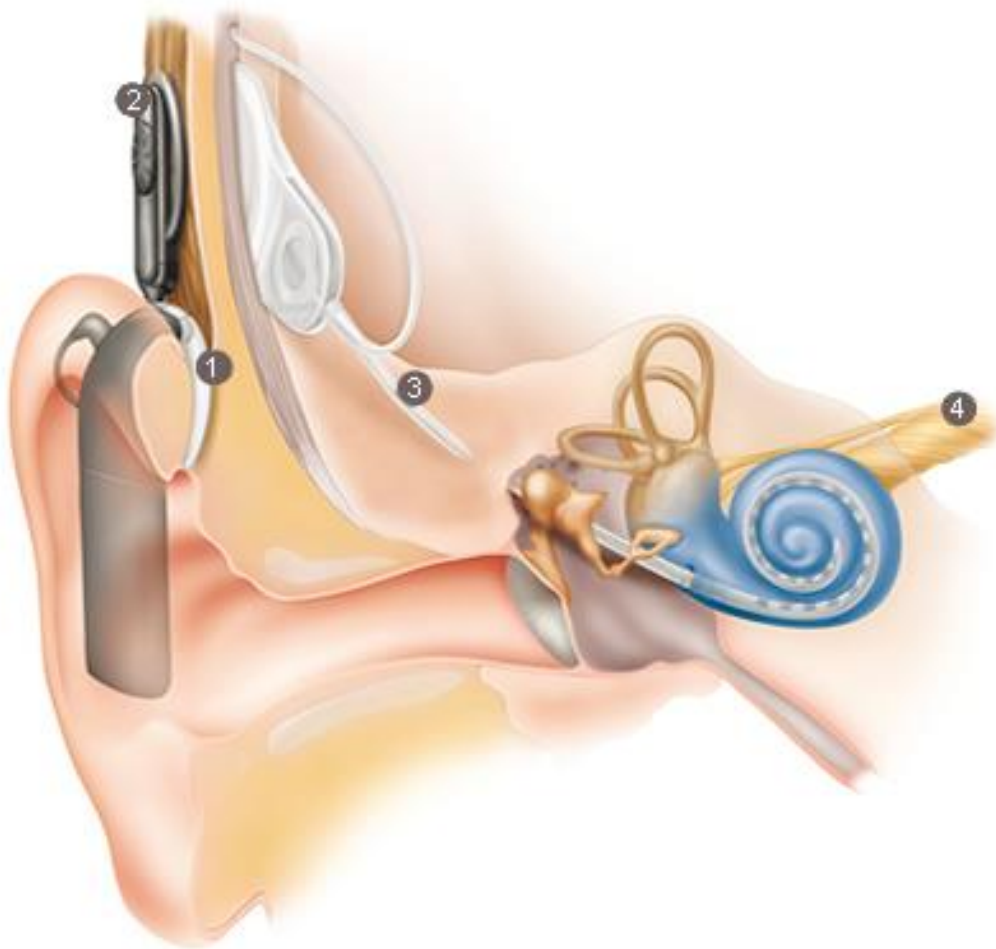
Figure 1.4 Diagram of cochlear implant in the human ear: (1) A sound processor transforms sound signals into a digital code, (2) A digital code is transmitted to the implant, (3) The implant converts a digital code into electrical signals and transfers them along the electrode array, (4) The electrodes stimulate the auditory nerves, which sends the electrical signals to the brain [26].

However, the conventional CI has some limitations; it needs extracorporeal devices, which expose a disability, require the relatively large power, frequent recharging and complicated signal processing circuits [19, 27, 28]. These limitations have been motivated many researchers to mimic the functions of cochlea and develop a fully implantable cochlear implant.

1.2 Numerous studies to mimic the functions of cochlea

Numerous studies have been conducted in order to overcome limitations of conventional cochlear implant systems. The fabricated artificial basilar membranes (ABMs) are divided in two types: membrane-type ABMs [9, 29-33] and beam array-type ABMs [27, 34-37].

The resonance frequencies of a membrane-type ABM vary depending on the width of the beams. A narrow membrane vibrates at high frequency, while a wide membrane senses low frequency. White and Grosh fabricated a micromachined cochlear model using polyimide membrane with silicon nitride (Si_3N_4) beams. The measured frequencies using acoustic stimulus were higher than the audible frequency range [9]. Shintaku *et al.* proposed a piezoelectric ABM which is made of a polyvinylidene difluoride (PVDF) membrane to mimic the function of the BM [29]. Chen *et al.* developed an artificial cochlea which is made of Cu beams on a piezoelectric membrane substrate using PVDF. The measured results showed strong longitudinal coupling on the ABM [30]. Zhou *et al*. reported a membrane-type ABM which is composed of two fluid-filled chambers separated by a polymer membrane [31]. Wittbrodt *et al.* also developed a polyimide membrane with Al beams using microfabrication methods to create life-sized physical models of the cochlea [32]. In our previous study, we compared the frequency selectivity of a membrane type ABM and beam array type ABM. We also determined that the frequency selectivity of a membrane type ABM is poor caused by the mechanical coupling of silicon dioxide (SiO$_2$) membrane [33].

The resonance frequencies of a beam array-type ABM vary depending on the length of the beams. A short beam vibrates at high frequency, while a long beam senses low frequency. Tanaka *et al.* developed a resonator array of silicon beams, which is named fishbone structure, as an artificial cochlear microphone. Its frequency selectivity was achieved by the different

beam lengths of the fishbone structure [34]. Xu *et al*. developed a polymeric micro-cantilever array as an acoustic sensors to mimic the biological front-end processing in the cochlea [35]. Kim *et al*. proposed an ABM consisting of an aluminum nitride (AlN) beam array with narrow supports to improve frequency separation. However, the piezoelectric signal of noise level was measured by deformation of beam caused by the narrow supports [36]. Jang *et al*. developed an AlN ABM beam array made of a silicon-on-insulator (SOI) wafer and deep reactive ion etching (DRIE) to improve the piezoelectric output compared with an ABM beam array of Kim *et al.* [27]. Jang *et al.* also developed a piezoelectric cantilever array using MEMS technology and evaluated its characteristics using animal tests [37].

Some ABMs have been fabricated using several piezoelectric materials because of its useful property, which is possible to convert acoustic energy into electrical energy without the energy supply. Chen *et al.* developed an ABM which is composed of Cu beams on a piezoelectric membrane substrate using PVDF [30]. Shintaku *et al.* proposed a piezoelectric ABM using PVDF membrane to mimic the function of the BM [29]. Lee et al. fabricated a trapezoidal silicone-based membrane using $Pb[Zr_xTi_{1-x}]O_3(PZT)$ thin film [38]. We have been fabricated beam array-type ABMs using AlN [27, 36, 37]. Because AlN is useful to fabricate an ABM; it can be integrated with complementary metal-oxide-semiconductor (CMOS) signal-processing technology and integrated-circuit (IC) processes [39].

To evaluate the properties of ABM in an environment that resembles the inside of cochlea, some experiments with fluidic chamber have been conducted. Zhou *et al.* and Wittbrodt *et al*. developed a membrane-type ABM which is made of two fluid-filled chambers separated by a polymer membrane as a model of the human cochlea [31, 32]. White and Grosh proposed a micro-engineered hydro-mechanical cochlear model with a fluid-filled duct that is similar to the mechanics of basilar membrane in cochlea [9]. Shintaku *et al*. proposed a

membrane type ABM using PVDF. It was measured in the liquid environment using silicon oil and fluidic chamber [29].

In our group, beam array-type ABMs using AlN have been researched to overcome the disadvantages of the conventional cochlear implant. Kim *et al*. proposed an ABM of AlN beam array with narrow supports to mimic the frequency separation function of the BM. The narrow supports were realized at both ends of the beams to lower the resonance frequencies by relaxing the fixed-fixed boundary conditions. However, the narrow supports leaded to rigid body motion of beams and the piezoelectric signal was too week as acoustic sensor [36]. To improve the piezoelectric voltage output, Jang *et al.* proposed an ABM composed of AlN beam array fabricated on a SOI wafer using DRIE. The ABM showed clear frequency selectivity and piezoelectric output [27]. Also, an AlN cantilever array was fabricated using MEMS technology and identified the characteristics such as frequency selectivity and piezoelectric output. The potential as CI applications of ABM was identified by using an animal model [37].

1.3 Objective of this research

In this paper, we proposed an the advanced MEMS artificial basilar membrane (ABM) fabricated on a silicon wafer using XeF_2 etching compared with the previous ABM beam array reported in Ref. [36]. It was improved as controlling the residual stress of beams using LPCVD Si_3N_4 and changing the dimension of open area to remove the narrow supports shown in the previous ABM of Kim *et al.*

Jang *et al.* fabricated an AlN ABM beam array using SOI and DRIE to overcome the limitations of the previous ABM of Kim *et al*. However, the production costs of an ABM proposed in Ref. [27] are rather expensive because of the high price of substrate, such as SOI wafer and the expensive process cost of DRIE. Its fabrication processes are complicated in comparison with XeF_2 etching. XeF_2 etching is cheaper than DRIE and a simple process that is purely chemical, because it uses a gas, XeF_2 for the etching silicon without plasma excitation in spite of its high etching rates [40]. Frequency selectivity and displacement to incoming sound pressure and electrical voltage were measured using Scanning Laser Doppler vibrometer (SLDV). Also, we experimentally evaluated and compared the characteristics of ABMs in air and fluid environment to identify the potential as total implantable devices.

2. DESIGN AND FABRICATIONS

2.1 Design of the advanced ABM

2.1.1 Theoretical calculation of the ABM

The ABM is designed to mimic the frequency separation function of the BM by changing the length of the beam based on the Euler-Bernoulli frequency theory. The resonance frequency is theoretically calculated from the following equation:

$$\mathfrak{f} = \frac{h\beta^2}{4\pi l^2} * \left(\frac{E}{3\rho}\right)^{0.5},$$
(2-1)

where E is Young's modulus of material composed of the beam, ρ is the density of the material composed of the beam. h, l represent the thickness, length, respectively. The value of β is assumed to be 4.73 for both the end fixed boundary condition and the first mode vibration [41]. ABM is consisted AlN and five different materials. Thus, a resonance frequency has to consider the properties of each material from Eq. (2-1). Young's modulus and density can be calculated as follow:

$$E = \sum_{k=1}^{n} E_k$$
(2-2)

$$\rho = \sum_{k=1}^{n} \rho_k$$
(2-3)

In Eqs. (2-2) and (2-3), k refers to the orders of material composed of the beam, and n refers to the number of material. A neutral axis can express the moment of inertia I_k, of each material based on Steiner's law.

$$c = \frac{\sum_{k=1}^{n} E_k Z_k h_k}{\sum_{k=1}^{n} E_k h_k} \qquad \textbf{(2-4)}$$

$$c_k = \frac{\sum_{k=1}^{n} h_k}{2} \qquad \textbf{(2-5)}$$

$$I_1 = \frac{1}{12} w h_1{}^3 + w h_1 (c - c_1)^2 \qquad \textbf{(2-6)}$$

$$I_2 = \frac{1}{12} w h_2{}^3 + w h_2 (c - c_2)^2 \qquad \textbf{(2-7)}$$

$$I_3 = \frac{1}{12} w h_3{}^3 + w h_3 (c - c_3)^2 \qquad \textbf{(2-8)}$$

In Eqs. (2-4)-(2-8), c is the neutral axis of a beam, w and h correspond to the width and thickness of material of a beam, respectively [42]. To avoid the position of neutral axis in piezoelectric material, the thicknesses of each material were determined by calculated result of neutral axis. The properties of each material in these formulas are referred to in table 2.1 [43-49]. The resonance frequency and neutral axis can be calculated using these properties.

Table 2.1 The properties of each material for the theoretical calculation of an ABM [43-49].

Material	Young's modulus (GPa)	Density (kg m^{-3})	Thickness (nm)
SiO$_2$	60	2200	500
LPCVD Si$_3$N$_4$	260.5	3000	500
Mo	312	10220	180
Ti	101.9	4430	20
AlN	340	3250	500
Au	130	19280	180

The range of calculated resonance frequencies is assumed from 0.5 to 3 kHz. Table 2.2 indicates the calculated resonance frequencies according to beam lengths. As the length of the beam increases, the resonance frequency decreases.

Table 2.2 The calculated lengths according to resonance frequencies.

Channel number	Beam length (μm)	The calculated resonance frequency (kHz)
1	1306	3.10
2	1338	2.91
3	1423	2.61
4	1516	2.30
5	1668	1.90
6	1818	1.60
7	1994	1.33
8	2323	0.98
9	2673	0.74
10	3194	0.52

Figure 2.1 shows the proposed schematic diagram of the advanced ABM using the XeF$_2$ etching. The array is composed of 10 beams, 300 μm in width. The lengths of the beams are varied sequentially from 1306 to 3194 μm, as shown in table 2.2. The structure is composed to multi-layer, an AlN layer, top electrode and bottom electrode. AlN is sandwiched in between the top electrode and bottom electrode.
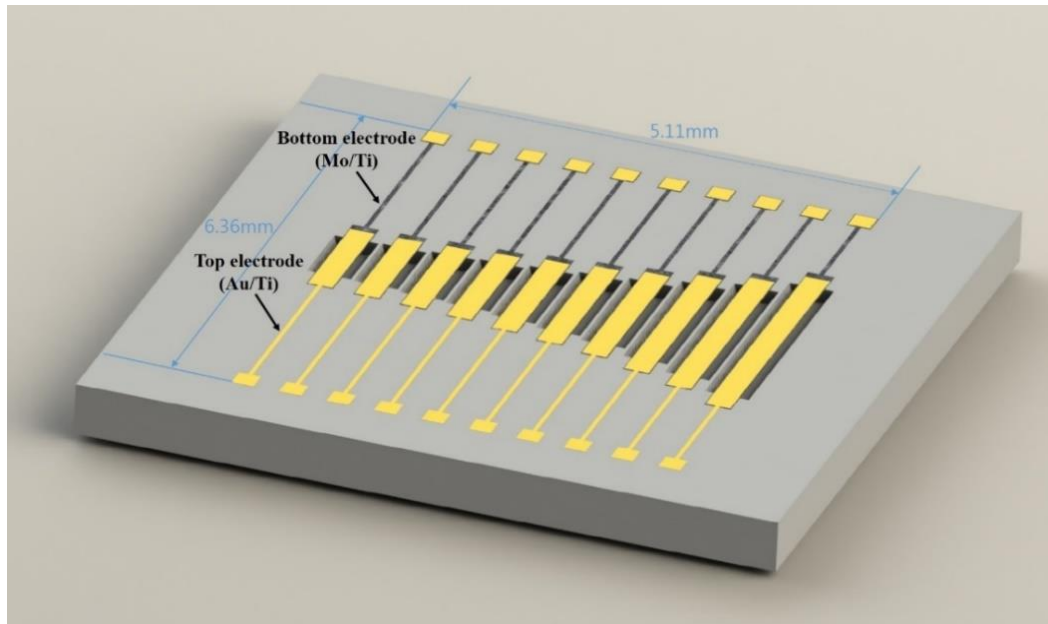
Figure 2.1 Schematic diagram of the advanced MEMS artificial basilar membrane using the XeF2 etching.

2.1.2 The advanced design of the ABM for removing narrow supports

The ABM of Kim et al. is realized at both ends of the beams to lower the resonance frequencies by relaxing the fixed-fixed boundary conditions. Due to the XeF_2 etching, the narrow supports were formed and the lateral deformation of the beam by the residual stress was observed. For this reason, the narrow supports led to rigid body motion of beams and the piezoelectric signal was too week as acoustic sensor [36].

To improve these problems, ABM is redesigned as changing the dimension of open area, as shown in figure 2.2. The dimension of open area is major factor in deciding the scope of etching. Hence, the gap both electrodes and open area is widened about 100 μm and the formation of narrow supports of the beam is prevented after the XeF_2 etching.
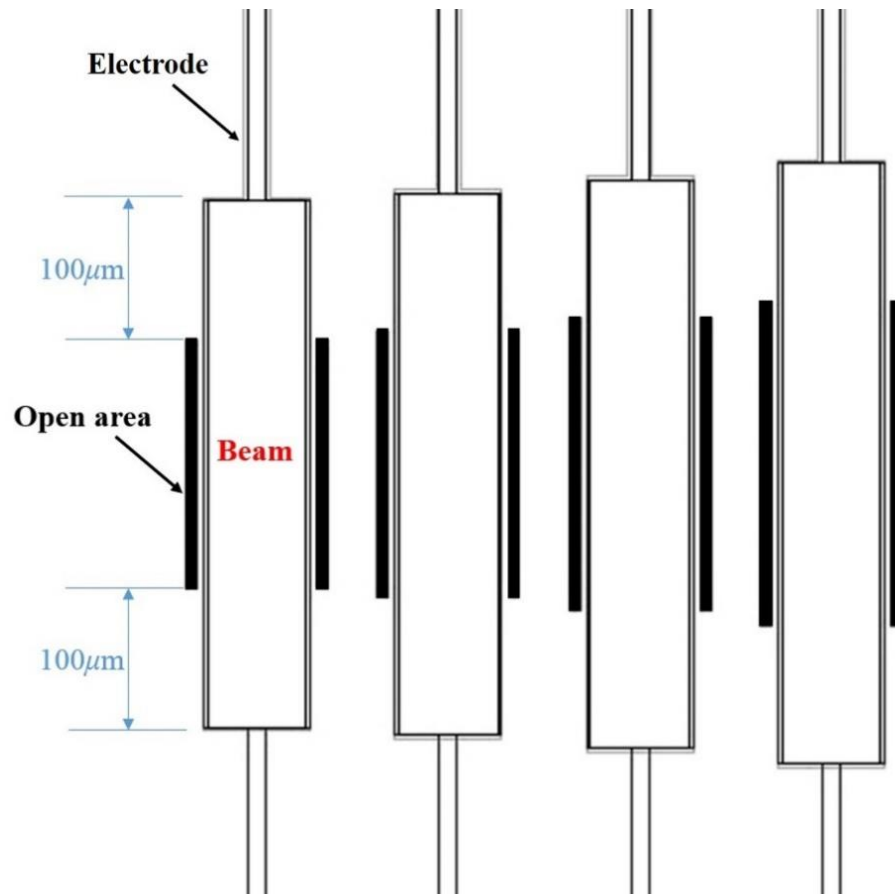
Figure 2.2 Design image of the advanced ABM for removing narrow supports.

2.2 Fabrication of the advanced ABM

2.2.1 The 1st fabrication process

By the previous formulas of neutral axis, we identified that a neutral axis of the ABM of Kim et al. is located in the piezoelectric material. To avoid the position of neutral axis in piezoelectric material, the thickness of SiO_2 was changed to 1.3 μm.
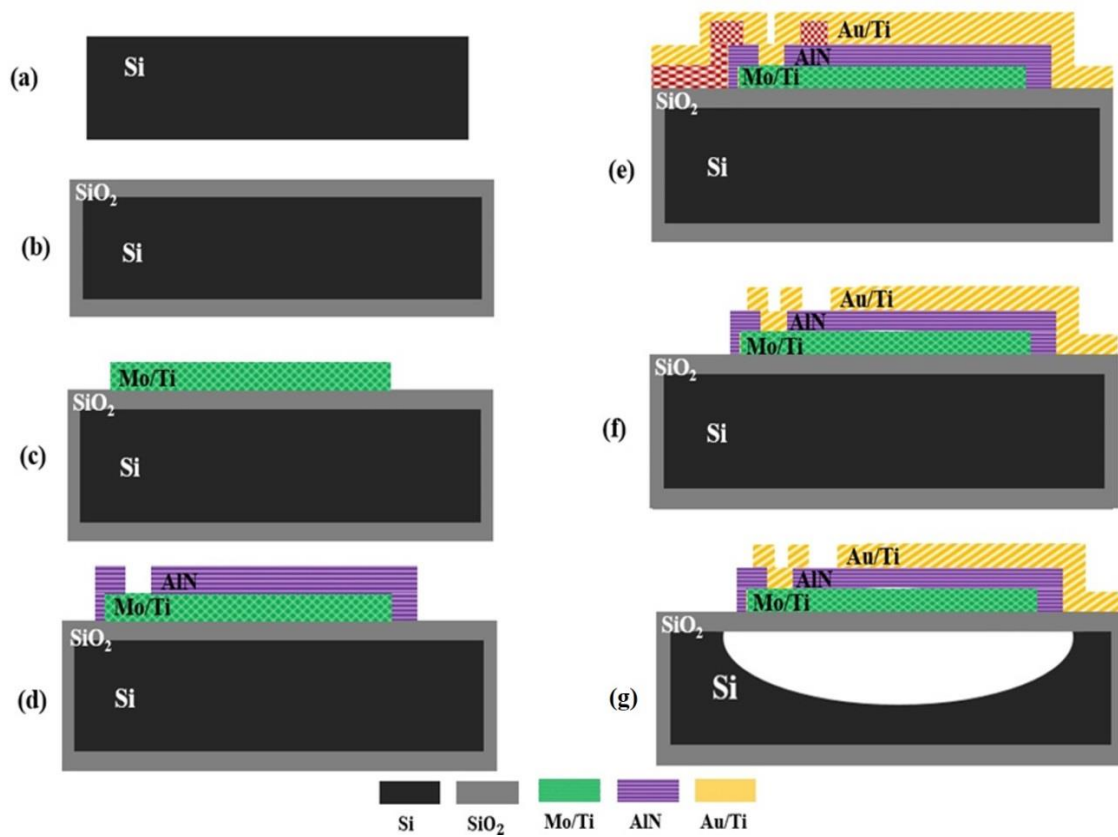
Figure 2.3 Flow diagram of the 1st fabrication process for a beam array of the advanced ABM: (a) A single-side, polished p-type (100) silicon wafer (diameter: 6 in.; thickness: 650 μm), (b) SiO2 was grown by thermal wet oxidation, (c) Mo/Ti was sputtered. The Mo bottom electrode was patterned and etched, (d) AlN was sputtered. The sputtered AlN was patterned and etched, (e) The lift-off process was conducted and Au/Ti was sputtered, (f) Au/Ti was patterned using acetone, and (g) A photolithography process was conducted on SiO2 and SiO2 was etched. Silicon was etched using XeF2 etcher.

Figure 2.3 shows the 1st fabrication process for a beam array of the advanced ABM. The materials of top and bottom electrode are gold and molybdenum (Mo). An aluminum nitride (AlN) is used as piezoelectric material. The fabrication process is equal to the ABM of Kim et al.'s. [36]. For device fabrication, we used a single-side, polished p-type (100) silicon wafer (diameter: 6 in.; thickness: 650 μm) as the substrate. (figure 2.3 (a)) On 6inch silicon wafer, the 1.3 μm thick SiO_2 was grown by thermal wet oxidation method at 1100℃. The parameters used for growth of SiO_2 are as shown in table 2.3. (figure 2.3 (b))

Table 2.3 Parameters used during the wet oxidation of 1.3μm thick SiO₂

Parameter	Value
Deposition thickness (Å)	13000
Temperature (℃)	1100
Gas composition O_2/H_2 (sccm)	8/5
Oxidation time (min)	390

Using the parameters shown in table 2.4, a 200nm thick Mo was sputtered. A 20nm thick titanium (Ti) was used as adhesive layer. The Mo bottom electrode was patterned by positive photolithography process using GXR601 photoresist and AZ300 developer. The detailed parameters used for patterning of the Mo bottom electrode are shown in table 2.5. The exposed part of the Mo bottom electrode was etched using an Al etchant. The etching conditions of Mo bottom electrode are indicated in table 2.6. Ti layer was etched by metal etcher using the parameters of table 2.7. (figure 2.3 (c))

Table 2.4 Parameters used during the deposition of Mo.

Parameter	Value
Deposition thickness (Å)	2000
Power (w)	400
Process pressure (mTorr)	5
Gas composition Ar (sccm)	150
Deposition time (sec)	450

Table 2.5 Parameters used for patterning of Mo bottom electrode.

Parameter	Value
Photoresist	GXR601
Spin speed and time	2000rpm for 5sec/4500rpm for 30sec/2000rpm for 5sec
PR thickness	1μm
Soft bake	90℃ for 1min
Expose	90mJ/cm^2
Develop	AZ300 developer, for 15sec
Rinse	DI water, for 30sec

Table 2.6 Parameters used during the wet etching of Mo.

Parameter	Value
Etchant	Aluminum etchant Type-A
Concentrations (%) (H_3PO_4: HNO_3: CH_3COOH : H_2O)	73 : 3.1 : 3.3 : 20.6
Temperature (℃)	25
Etching time (sec)	300

Table 2.7 Parameters used during the RI etching of Ti.

Parameter	Value
RF power (w)	400
Bias Power (w)	100
Process pressure (mTorr)	5
Gas composition Cl_2 (sccm)	40
Etching time (sec)	35

After the AlN of 500nm thickness was sputtered, it was patterned by negative photolithography process using AZ5214 photoresist and CD30 developer. The detailed parameters used for patterning of the AlN are shown in table 2.8. Using the parameters shown in table 2.9, the AlN was etched by metal etcher using Cl_2 and Ar mixed gas. (figure 2.3 (d))

Table 2.8 Parameters used for patterning of AlN.

Parameter	Value
Photoresist	AZ5214
Spin speed and time	1500rpm for 5sec/2500rpm for 25sec/1500rpm for 5sec (double coating)
PR thickness	1.8μm
Soft bake	90℃ for 20min
Expose	200mJ/cm^2
Post bake	120℃ for 1min
Post exposure	3500mJ/cm^2
Develop	CD30 developer, for 25~30sec
Rinse	DI water, for 30sec
Hard bake	120℃ for 45sec

Table 2.9 Parameters used during the RI etching of AlN.

Parameter	Value
RF power (w)	800
Bias Power (w)	50
Process pressure (mTorr)	5
Gas composition Cl_2/Ar (sccm)	60/10
Etching time (sec)	600

For lift off process of top electrode, AZ5214 photoresist and CD30 developer were used for the process. The detailed parameters of photolithography process are shown in table 2.10. Using the parameters shown in table 2.11 and 2.12, a 200nm thick gold and 20nm thick Ti were deposited by evaporator. (figure 2.3 (e)) To pattern the top electrode, a gold top electrode and Ti were lift off using acetone and ultrasound. (figure 2.3 (f))

Table 2.10 Parameters used during the lithography process for lift off.

Parameter	Value
Photoresist	AZ5214
Spin speed and time	2500rpm for 5sec/3500rpm for 25sec/2500rpm for 5sec
PR thickness	1μm
Soft bake	90℃ for 1min
Expose	90mJ/cm^2
Post bake	120℃ for 45sec
Post exposure	2520mJ/cm^2
Develop	CD30 developer, for 15sec
Rinse	DI water, for 30sec
Hard bake	120℃ for 45sec

Table 2.11 Parameters used during the deposition of Au using evaporator.

Parameter	Value
EB-voltage (kV)	10
EB-current (mA)	65
Deposition rate (Å /sec)	1

Table 2.12 Parameters used during the deposition of Ti using evaporator.

Parameter	Value
EB-voltage (kV)	10
EB-current (mA)	72
Deposition rate (Å /sec)	1~1.5

A SiO_2 was patterned by photolithography process using AZ5214 photoresist and CD30 developer. The parameters used for patterning of SiO_2 are equal to them used for patterning of AlN. Using the parameters shown in table 2.13, the exposed SiO_2 was etched by ICP RIE to make open area for gas flow of the XeF_2 etcher. Isotropic silicon etching was performed using a XeF_2 etcher. The parameters used during silicon etching are as shown in table 2.14. (figure 2.3 (g))

Table 2.13 Parameters used during the ICP etching of 1.3μm thick SiO_2.

Parameter	Value
RF power (w)	950
Bias Power (w)	100
Process pressure (mTorr)	2
Gas composition CHF_2 /CF_4 (sccm)	30/20
Etching time (sec)	420

Table 2.14 Parameters used during the XeF$_2$ etching of Si.

Parameter	Value
Process pressure (Torr)	5
Gas composition N$_2$/XeF$_2$ (sccm)	50/10~11
Etching time (sec)	7200

The fabricated sample is shown in figure 2.4. As shown in figure 2.4, the residual stresses generated during the MEMS fabrication process. Most of the beams were broken on the way to the XeF$_2$ etching and the deformation of the beams was observed after releasing the beam. That is, this fabrication ended in failure.
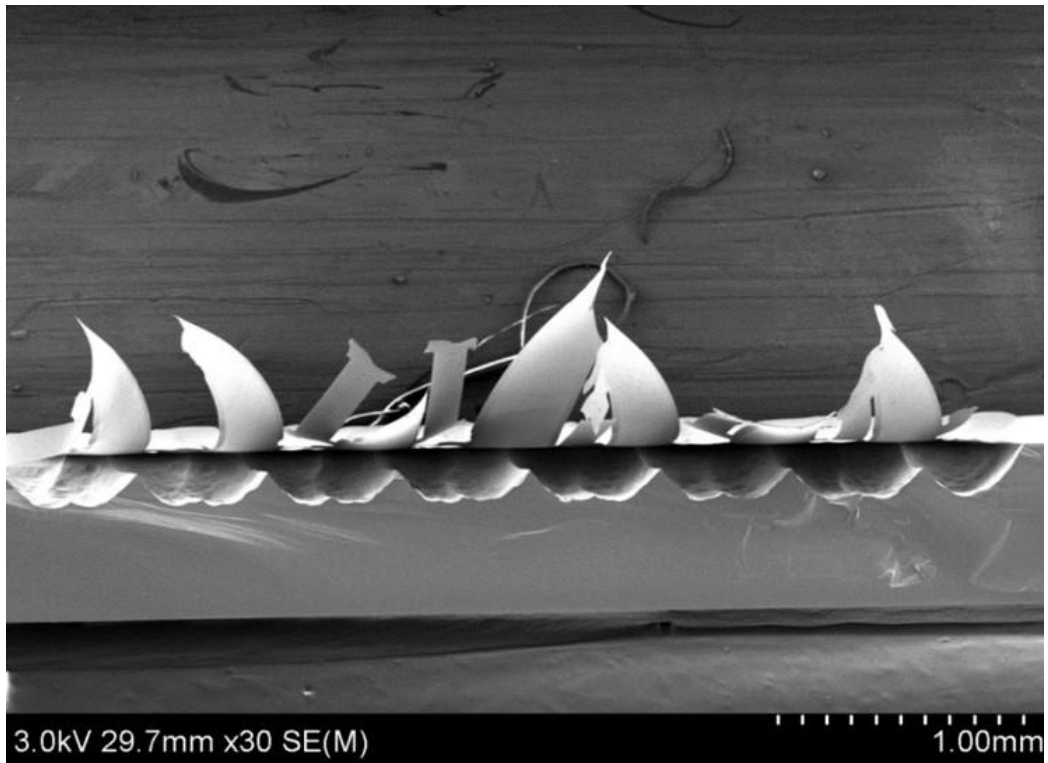
(a)
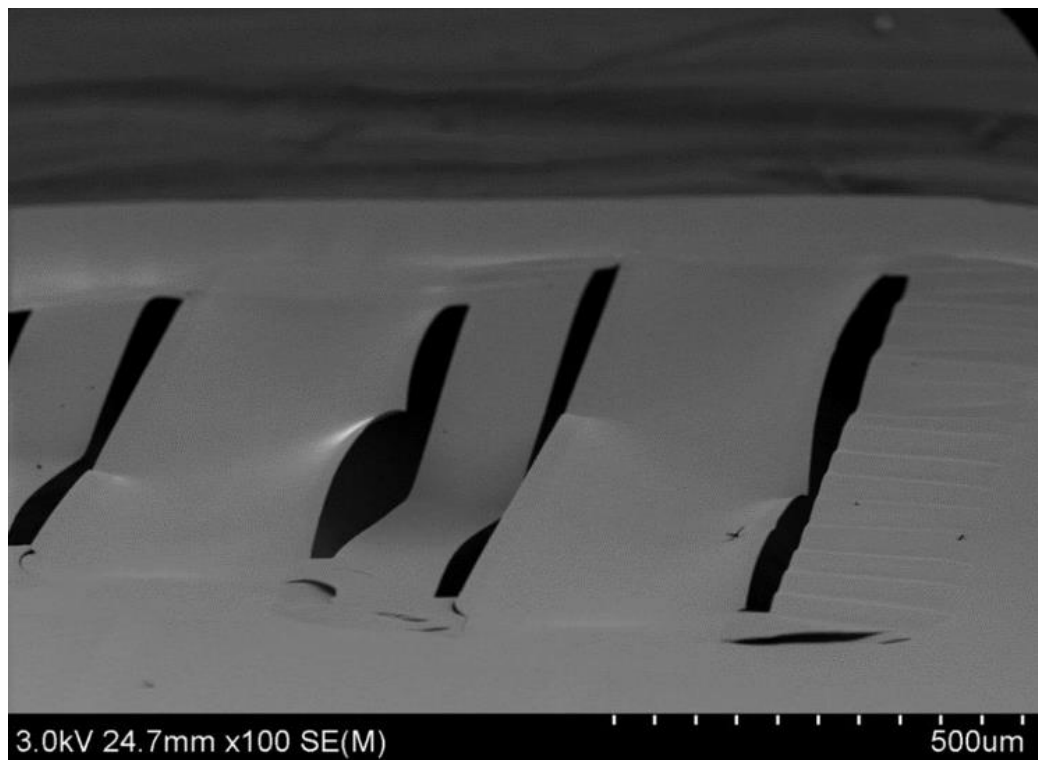
(b)

Figure 2.4 SEM images of the fabricated sample through the 1st fabrication process.

2.2.2 The 2nd fabrication process

To reduce the residual stress of the beam, we determined to reduce the thickness of SiO_2 by 500nm and to add a 500nm thick LPCVD Si_3N_4 at the same time. Because a tensile stressed LPCVD Si_3N_4 is used to compensate for the compressive stress of a SiO_2 [45].
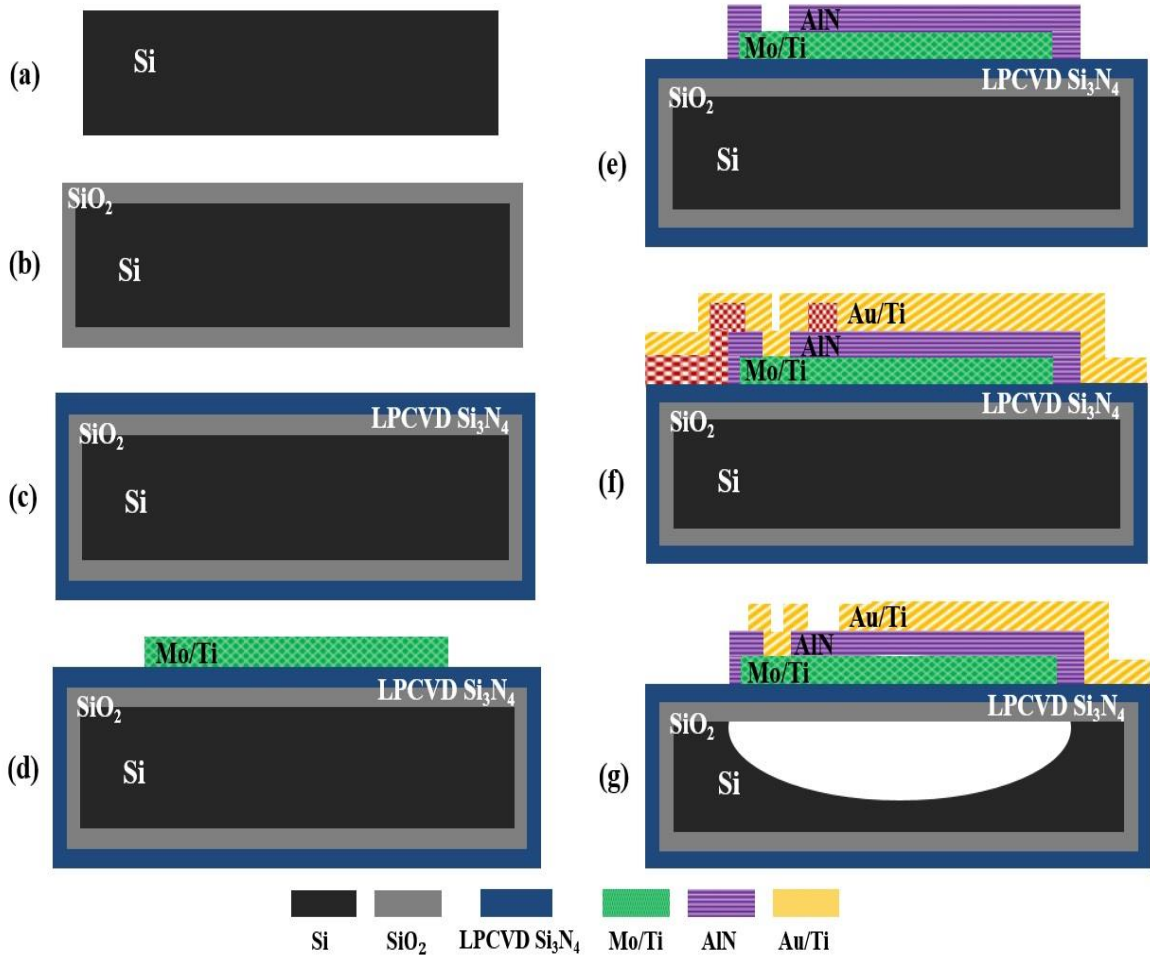
Figure 2.5 Flow diagram of the 2nd fabrication process for a beam array of the advanced ABM: (a) A single-side, polished p-type (100) silicon wafer (diameter: 6 in.; thickness: 650 μm), (b) SiO2 was grown by thermal wet oxidation, (c) LPCVD Si3N4 was deposited by LPCV, (d) Mo/Ti was sputtered. The Mo bottom electrode was patterned and etched, (e) AlN was sputtered. The sputtered AlN was patterned and etched, (f) The lift-off process was conducted. Au/Ti was sputtered, and (g) Au/Ti was patterned using acetone. A photolithography process was conducted on the LPCVD Si₃N₄ and LPCVD Si₃N₄ and SiO₂ were etched. Silicon was etched using XeF₂ etcher.

Figure 2.5 shows the 2nd fabrication process for a beam array of the advanced ABM. The fabrication process is similar to the 1st fabrication process, but two additional processes have to be considered; After thermal wet oxidation of SiO_2 using the parameters shown in table 2.15, LPCVD Si_3N_4 was deposited by LPCVD, as shown in figure 2.5 (c).

Table 2.15 Parameters used during the wet oxidation of 500nm thick SiO₂.

Parameter	Value
Deposition thickness ($\mathring{A}$)	5000
Temperature (℃)	1100
Gas composition O_2/H_2 (sccm)	8/5
Oxidation time (min)	64

After the lift-off process to pattern the top electrode, A LPCVD Si_3N_4 was patterned by photolithography process using AZ5214 photoresist and CD30 developer. The LPCVD Si_3N_4 and SiO_2 were sequentially etched using ICP RIE for the XeF_2 etching. The detailed parameters used for etching of the LPCVD Si_3N_4 and SiO_2 are shown in table 2.16 and 2.17.The beams were released by etching the silicon using a XeF_2 etcher. (figure 2.5 (g))

Table 2.16 Parameters used during the ICP etching of 500nm thick SiO₂.

Parameter	Value
RF power (w)	950
Bias Power (w)	100
Process pressure (mTorr)	2
Gas composition CHF_2/CF_4 (sccm)	30/20
Etching time (sec)	160

Table 2.17 Parameters used during the ICP etching of 500nm thick Si$_3$N$_4$.

Parameter	Value
RF power (w)	700
Bias Power (w)	80
Process pressure (mTorr)	2
Gas composition CF$_4$/O$_2$ (sccm)	25/8
Etching time (sec)	140

Figure 2.6 shows the optical images of two piezoelectric beam arrays using XeF$_2$ etching: a wide- supports beam array (WSBA) and a narrow-supports beam array (NSBA). For clear comparison of two beam arrays, the advanced ABM was named the WSBA. Also, the previous ABM of Kim et al. was named the NSBA. [2-7]. Figure 2.6 (a) shows an optical image of the WSBA, which was consisted of 10 beams. Figure 2.6 (b) shows a removed narrow support of a beam by the widening gap of between electrode and open area. The NSBA is shown in Figure 2.6 (c) - (d). The narrow support led in the deformation of beam. As shown in figure 2.7, there is little deformation of a beam in the WSBA by the compensation of SiO$_2$ and LPCVD Si$_3$N$_4$.
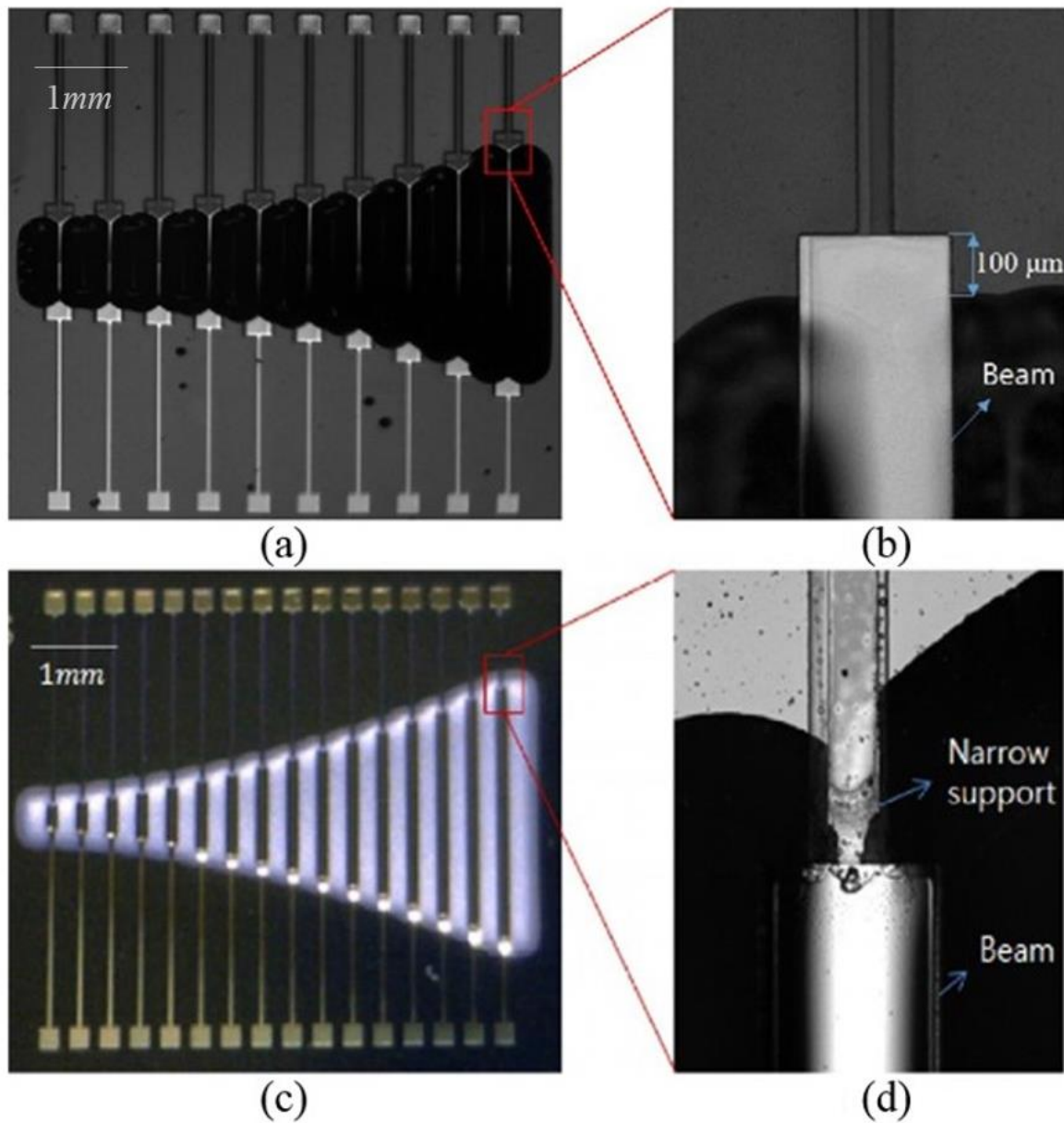
Figure 2.6 Comparison between the WSBA and the NSBA: (a) Optical image of the WSBA, (b) A close-up image of the WSBA; a removed narrow support by improved design, (c) Optical image of the NSBA, and (d) A close-up image of the NSBA; a narrow support and deformation of beam [36].
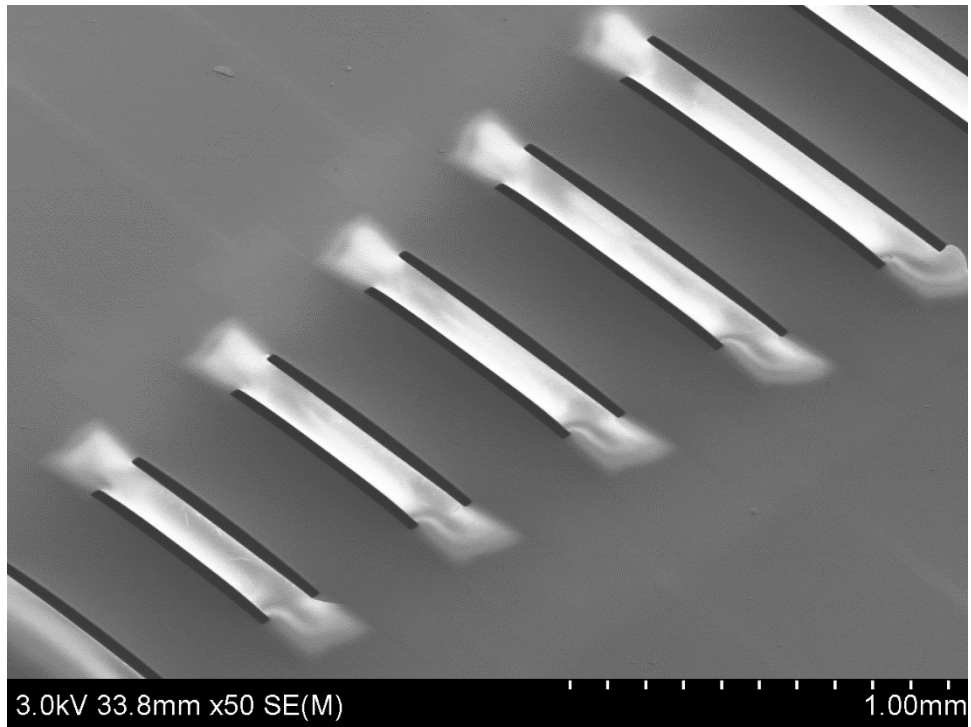
(a)
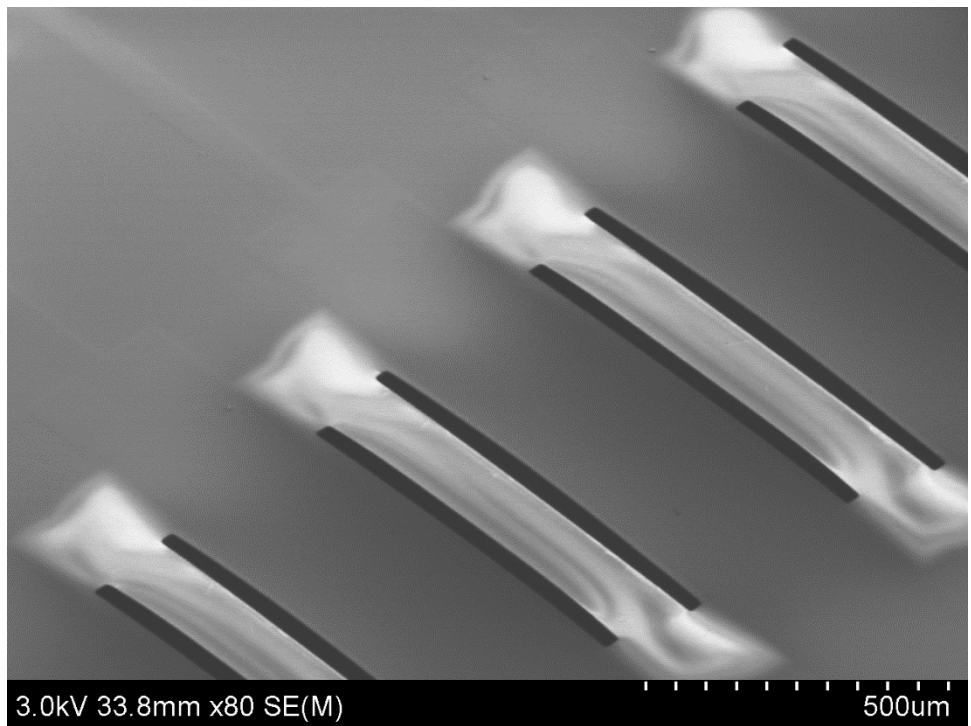
(b)

Figure 2.7 SEM image of the advanced ABM.

3. EXPEREIMENT SETUP

3.1 Measurement setup using SLDV

The vibrating characteristics of the ABM were measured using an MSA-E-500 microsystem analyzer (Polytec GmbH, Germany) integrated with a scanning laser-Doppler vibrometer (SLDV) for acoustic and electric stimulus. The experiments were conducted in an anechoic chamber with a background noise level of 18.7 dB. Each beam was excited by acoustic and electric waveforms of periodic chirp generated from the SLDV control module. Figure 3.1 shows the experimental setup for measurement in an anechoic chamber. Figure 3.2 shows a schematic of experimental setup for measurement of vibrating characteristics of ABM using acoustic and electric stimulus. The sound pressure from a loudspeaker (A7X, Adam, Germany) was used as the acoustic stimulus. The speaker was inclined at ~40° with respect to

the surface of the samples due to space limitations. The input sound pressure was measured using a reference microphone (4189, Bruel and Kjaer, Germany). It placed close to the device. The sound pressure lever (SPL) for the measurements was approximately 100~105dB. For the electric stimulus, an AC with a 1 V amplitude was applied by an MSA-E-500 junction box (Polytec, Germany) to flow through the AlN layer. To determine the resonance frequencies and displacement of the beam using the SLDV, sufficient measuring points were distributed on the surface of each beam. The number of measuring points was altered accordingly from 90 to 120, depending on the length of the beam. Both ends of each beam attached with silicon were excepted from the measurement. At each measurement point, 20 output datasets were collection to obtain averaged data. In air, acoustic stimulus of periodic chirp with frequency range of 500 Hz – 40 kHz were applied using a loudspeaker. Because the limitation of a loudspeaker was until 40 kHz. In electric stimulus, the frequency range of periodic chirp was

500 Hz – 100 kHz. The frequency range was widely set for identifying the vibrating characteristics of beams which have frequencies of above 40 kHz. The sampling frequency was 102.4 kHz, and the sampling time was 160ms. Also, the piezoelectric output from each beam was measured using a data acquisition system (DAQ) connected to the SLDV.
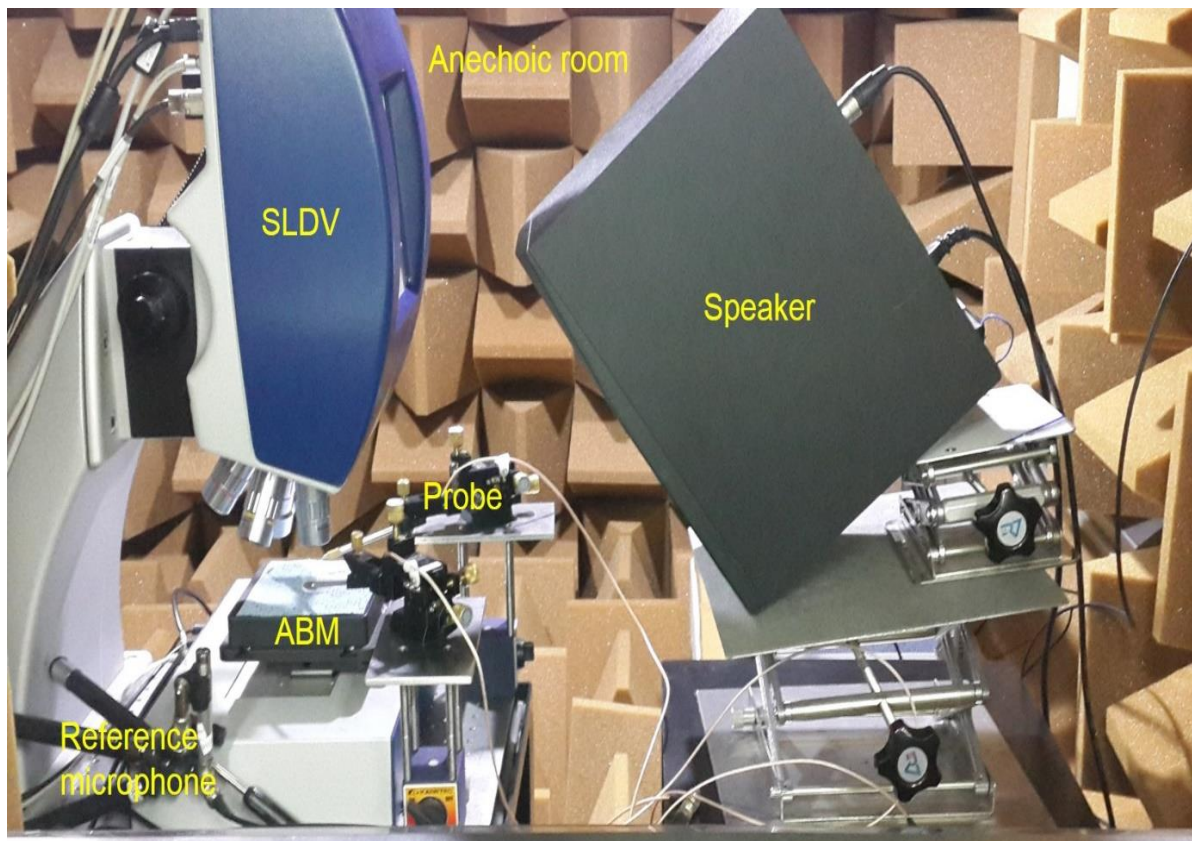
Figure 3.1 Experimental setup for measurement in an anechoic chamber.
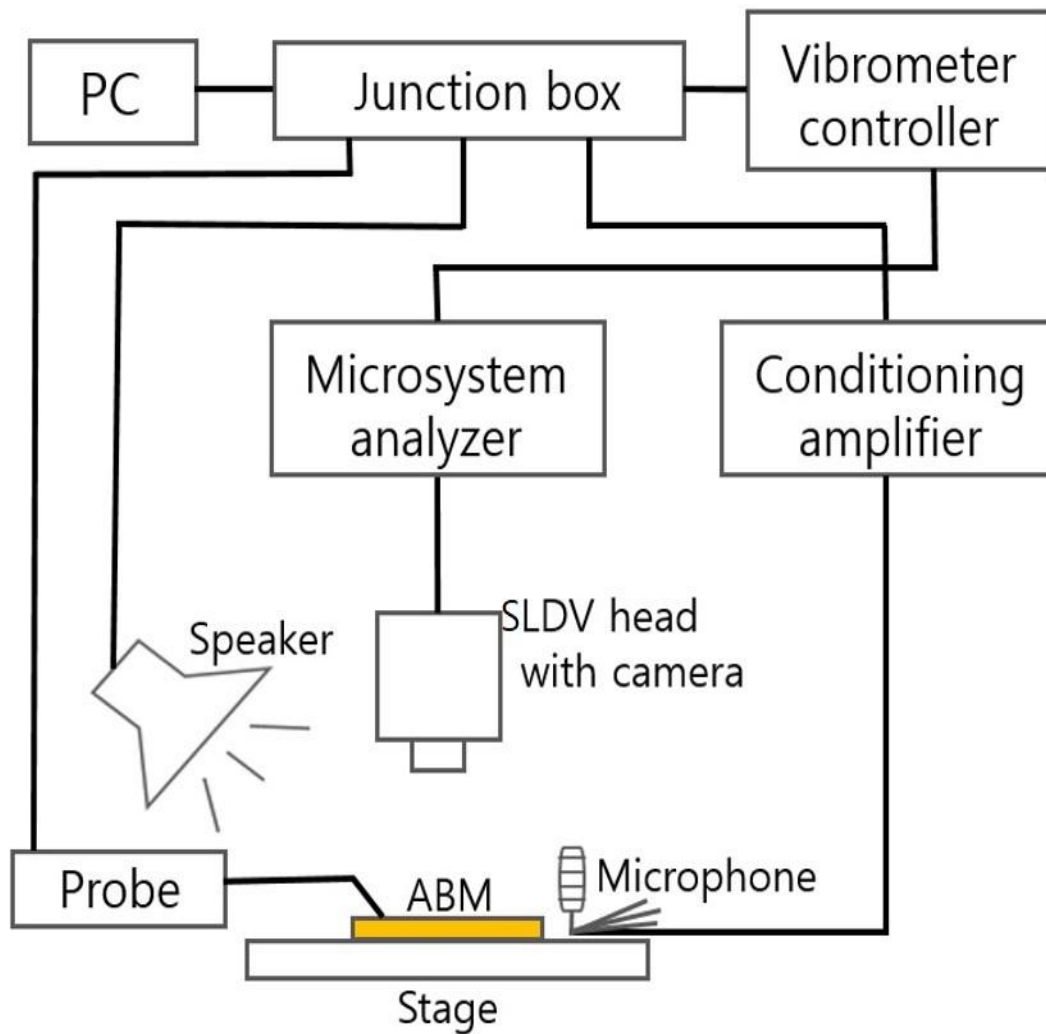
Figure 3.2 Schematic of experimental setup for measurement of vibrating characteristics of ABM using acoustic and electric stimulus.

After satisfying the aforementioned conditions for measurement of vibrating characteristics of the ABM using acoustic stimulus, the measurement was performed. When the acoustic stimulus with frequency range of 500 Hz – 40 kHz was applied using a loudspeaker, the beam was vibrating at the corresponsive frequency band. The vibrating characteristics of ABM such as displacement and resonance frequency are measured by a laser of SLDV. The piezoelectric voltage was measured by two probe tips placed on top and bottom electrodes for acoustic stimulus. Figure 3.3 shows the input sound pressure in time (figure 3.3 (a)) and frequency domain (figure 3.3 (b)).

(a)

(b)
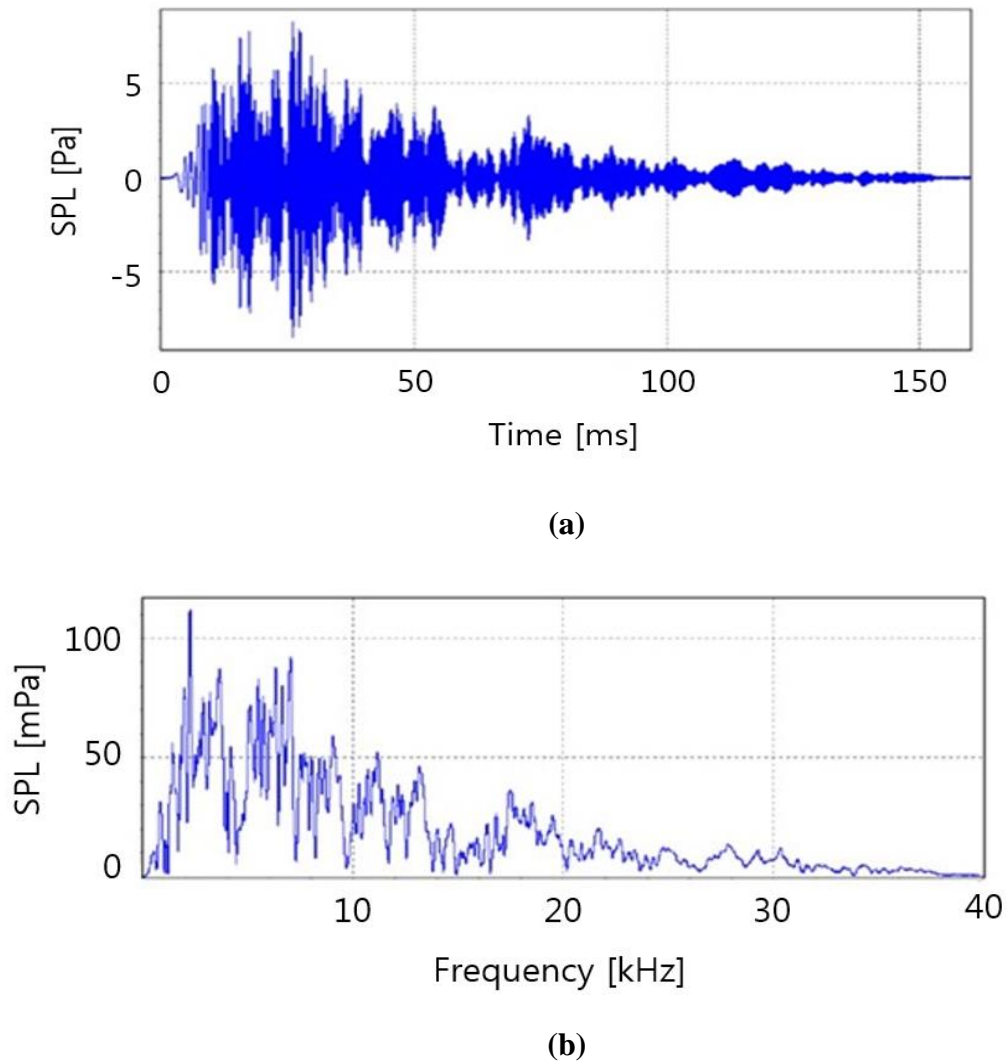
Figure 3.3 Input sound pressure (a) in time domain and (b) frequency domain.

We can identify the vibrating characteristics of ABM using the converse piezoelectric effect. Because the mechanical deformation in a piezoelectric material happens when an electric field is applied to electrodes of ABM. Most of the measurement environment is similar to that for acoustic stimulus. But, an input signal is changed from acoustic signal to electric signal. Thus, two probe tips were placed on top and bottom electrodes. An AC with 1 V stimulus was applied using probe tips, the vibrating characteristics of ABM were measured by a laser of SLDV. Figure 3.4 shows the input sound pressure in time (figure 3.4 (a)) and frequency domain (figure 3.4 (b)).
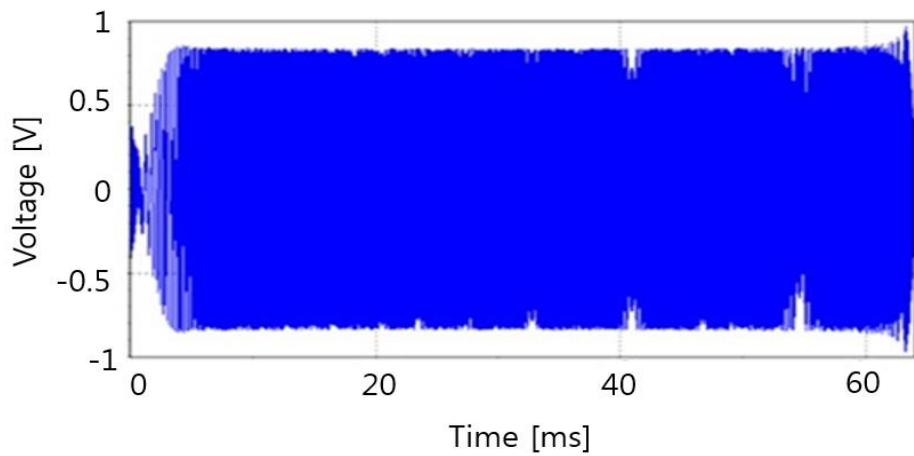

(a)
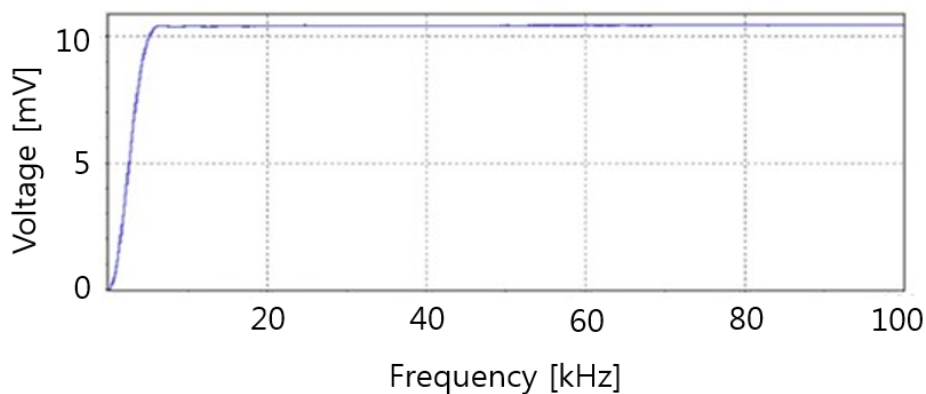
(b)

Figure 3.4 Input voltage (a) in time domain and (b) frequency domain.

3.2 Measurement setup in fluid

Figure 3.5 shows the experimental setup for measurement in fluid. The displacement with the resonance frequencies in fluid environment was measured by soaking the ABM in DI water. The petri dish was used instead of the fluidic chamber. The ABM sample was fixed by sticky tape in the petri dish, whose diameter is 50mm. The petri dish containing the sample was also fixed using sticky tape on the stage. The water of 8ml, which is the required amounts to cover the ABM completely, was dropped by a pipette in the petri dish as shown in figure 3.6. The experiment in fluid was conducted by applying an AC with a 1 V amplitude using by an MSA-E-500 junction box (Polytec, Germany) and the probe tips. The displacement of the beam at the resonance frequencies was determined by the laser of SLDV. The obtained average data was seen on the connected monitor.
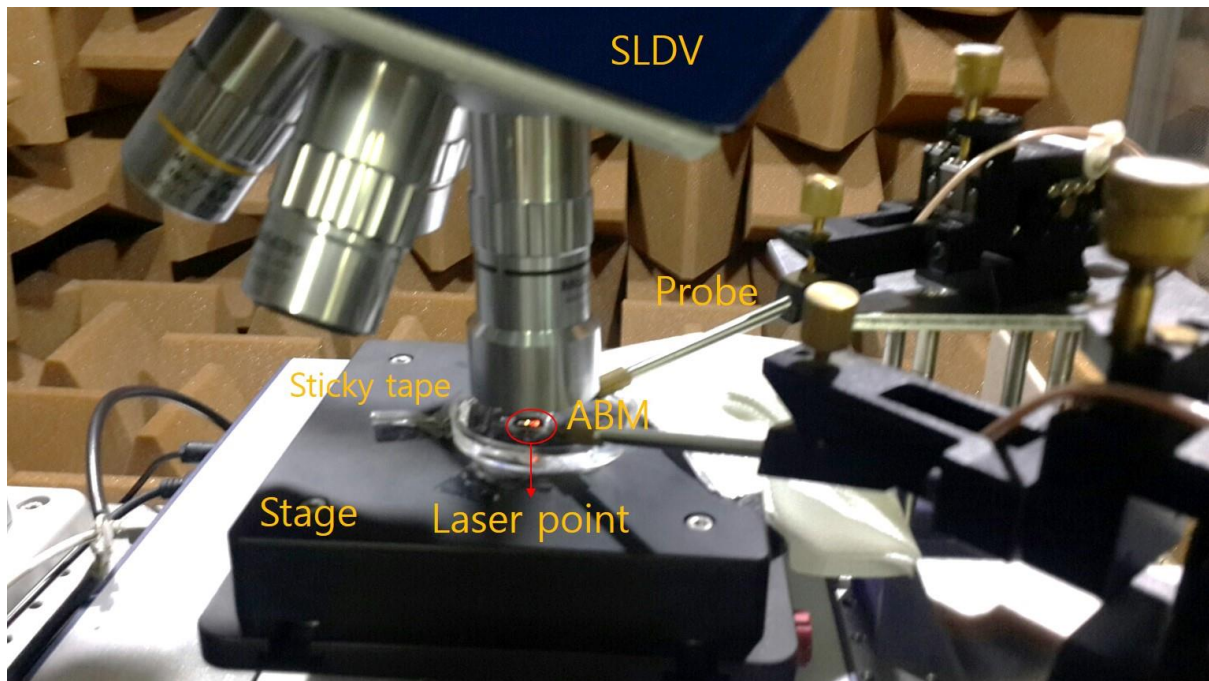
Figure 3.5 Experimental setup for measurement of an ABM in fluid.
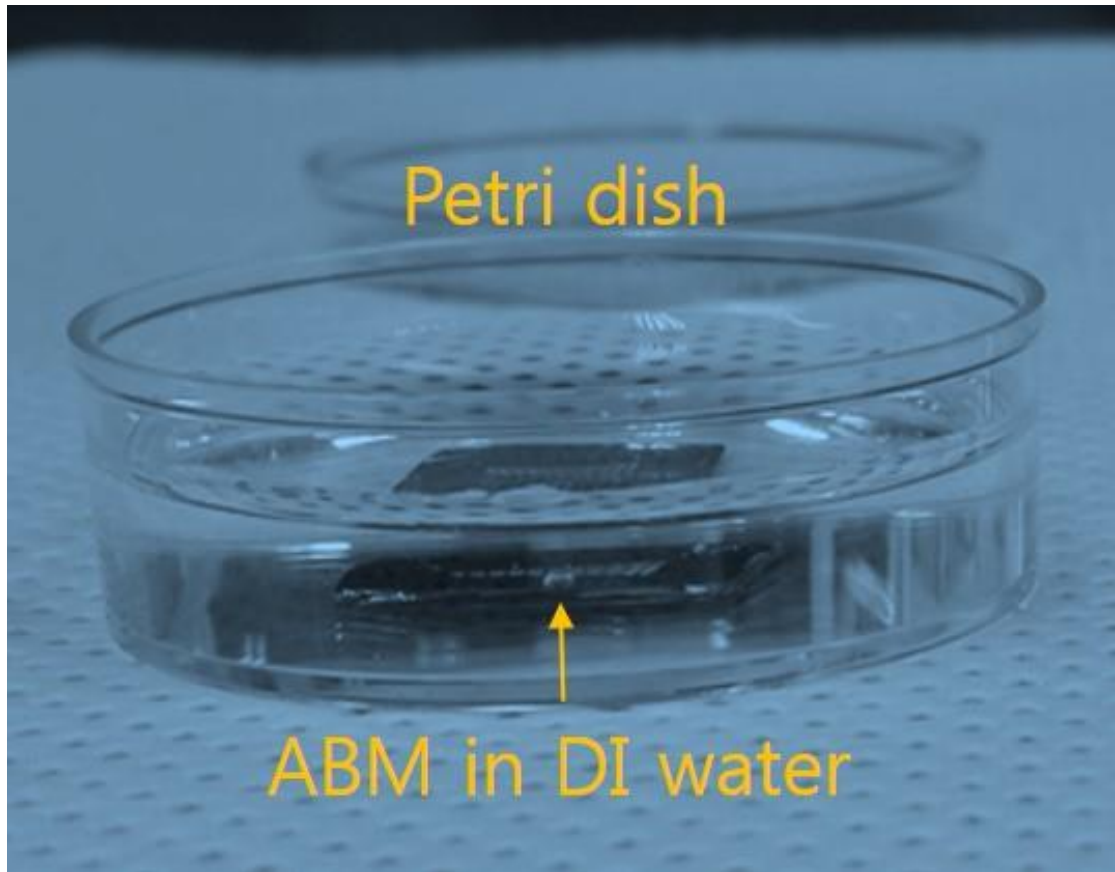
Figure 3.6 ABM in DI water.

4. Measurement results and discussions

4.1 Performance characteristics of the ABM in air

4.1.1 Mechanical responses of the ABM

When the acoustic stimulus was applied using a loudspeaker, the beams were vibrating at the corresponding resonance frequency, as shown in figure 4.1. The images of figure 4.1 show the vibrational modes of two piezoelectric beam arrays using XeF_2 etching: a wide-supports beam array (WSBA) and a narrow-supports beam array (NSBA). While the WSBA showed the 1st bending mode clearly in figure 4.1(a), the NSBA had the rigid body motion caused by the narrow supports at both sides of the beam, as shown in figure 4.1(b) [36].
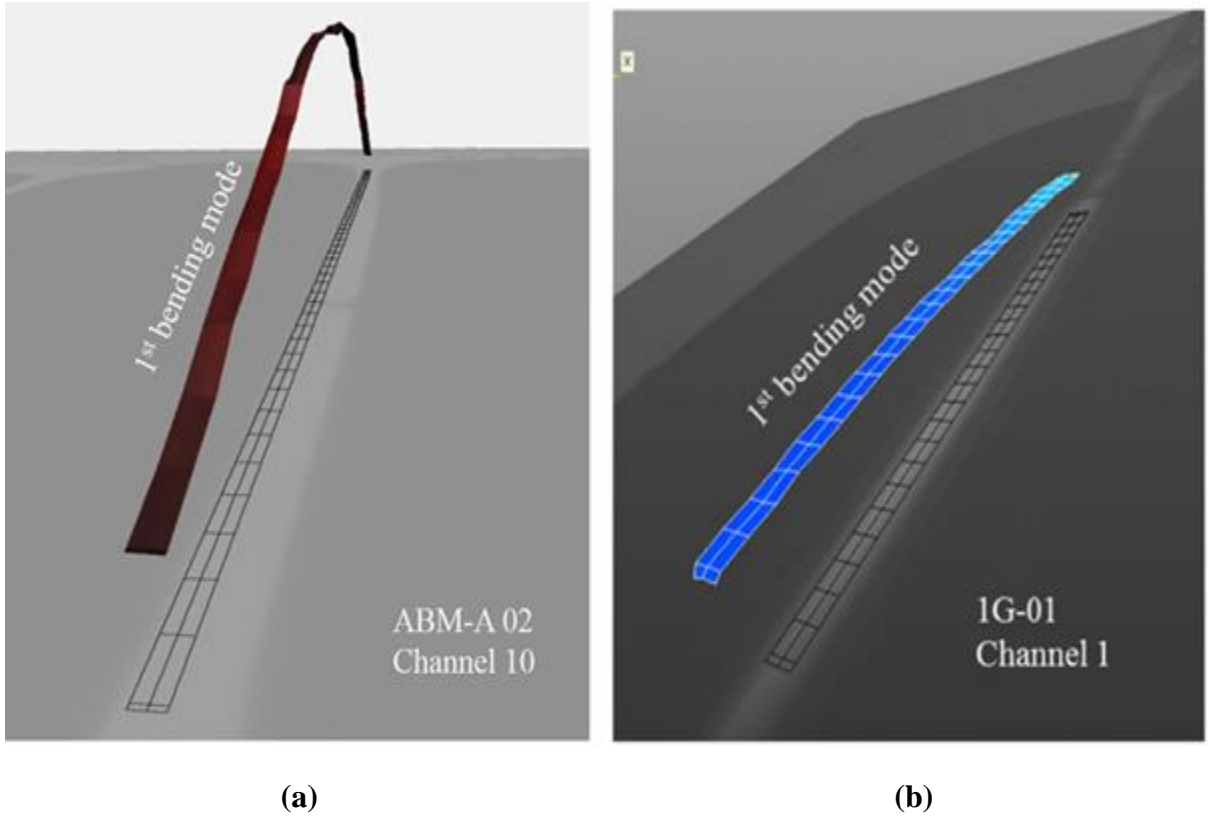

(a)   (b)

Figure 4.1 Beam deflection imaged using SLDV: (a) Channel 10 of the WSBA, and (b) Channel 1 of the NSBA [36].

Acoustic or electric stimulus tests were conducted for ABM-A 02, ABM-A 08, and ABM-A 09. Table 4.1 shows the mean resonance frequencies per each beam length in three samples during acoustic or electric stimulus in air. Acoustic stimulus tests were conducted from channel 4 to channel 10. Because the frequency band of a loudspeaker had a limitation up to 40 kHz. Thus, the beams which have a certain frequency above 40 kHz was not measured using acoustic stimulus. The unmeasured values was marked as 'N/A'.

Table 4.1 Mean resonance frequencies per each beam length in three samples for acoustic or electric stimulus in air.

Channel number	Beam length [μm]	Acoustic stimulus tests	Electric stimulus tests
		Mean resonance frequency [kHz]	Mean resonance frequency [kHz]
1	1306	N/A	47.648
2	1338	N/A	44.703
3	1423	N/A	41.235
4	1516	36.535	37.193
5	1668	30.931	31.385
6	1818	26.310	27.380
7	1994	22.969	23.588
8	2323	17.862	18.719
9	2673	13.956	14.891
10	3194	10.508	11.078

N/A; Measurement was not conducted due to the limitation of a loudspeaker.

The measured displacement showed a similar frequency response at the geometric center of beams, as shown in Figure 4.2. Figure 4.2 (a) shows the displacement from channel 4 to channel 10 of sample ABM-A 02 measured by acoustic stimulus. The maximum displacement of the beams for acoustic stimulus was in the range 0.5 – 3.2 nm shown in figure 4.2 (a). The displacement of all the beams measured by electric stimulus was shown in figure 4.2 (b). The maximum displacement of the beams for electric stimulus was in the range 10 – 40 nm shown in figure 4.2 (b). The peak of each beam represented the resonance frequency at the first longitudinal bending mode. The peaks shifted toward lower frequencies as the beam length increased.
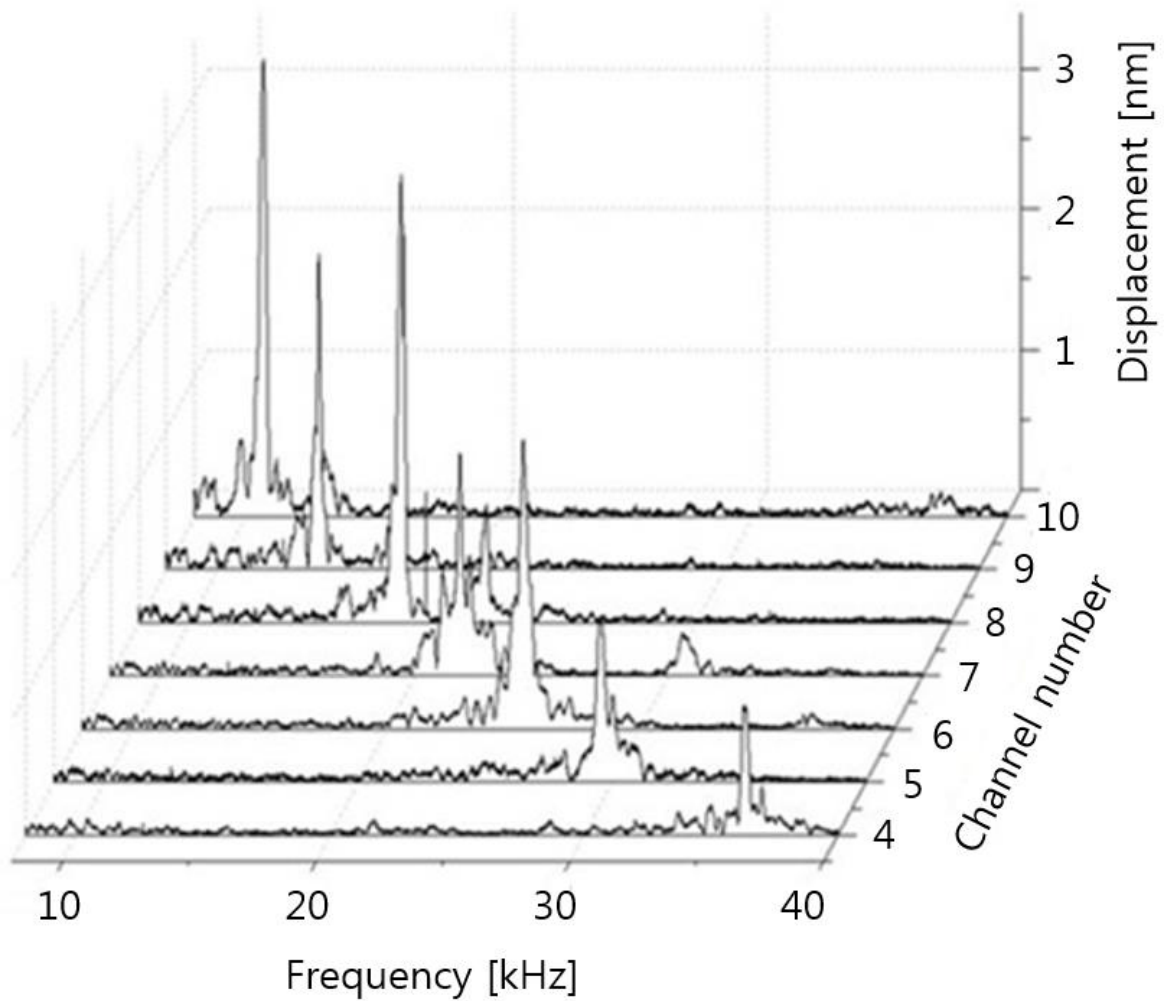

(a)
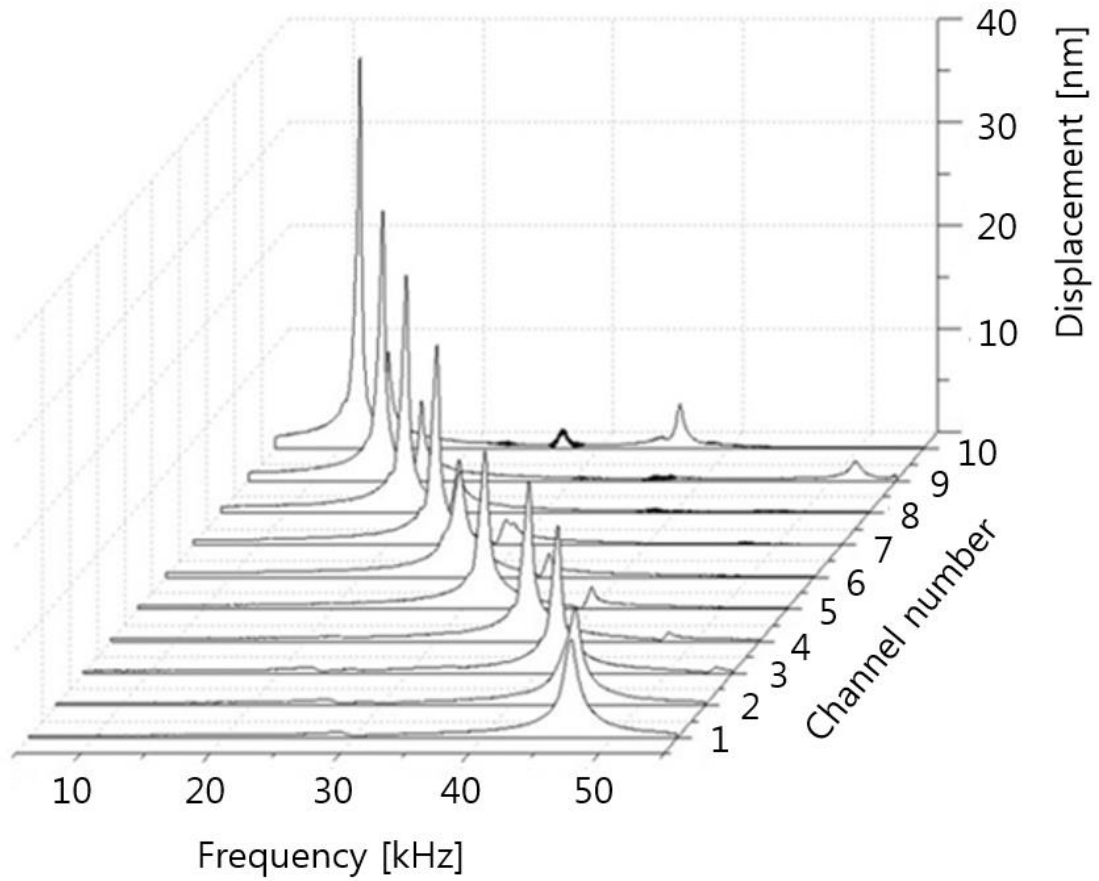
(b)

Figure 4.2 Displacement of the beams in the array for sample ABM-A 02: (a) during acoustic stimulus, and (b) during electric stimulus.

An electro-mechanical transfer function (H_{VD}) was defined as the ratio of displacement output to the voltage input. An acoustic-mechanical transfer function (H_{PD}) was defined as the radio of displacement output to the sound pressure input. However, an acoustic stimulus which has the frequency above 20 kHz was not measured using microphone. The accurate acoustic-mechanical transfer function (H_{PD}) was not obtained. Therefore, the measured displacements of beams were standardized by the applied voltage. Magnitude of the transfer function in the frequency range of 500 - 40,000 Hz, measured with electric stimulus is shown in figure 4.3. The maximum magnitude of the transfer function for electric stimulus was in the range 0.8 –

3.5 µm/V. During the electric stimulus, the peak of the transfer function sequentially moved

toward the lower frequency region as the beam length increased.
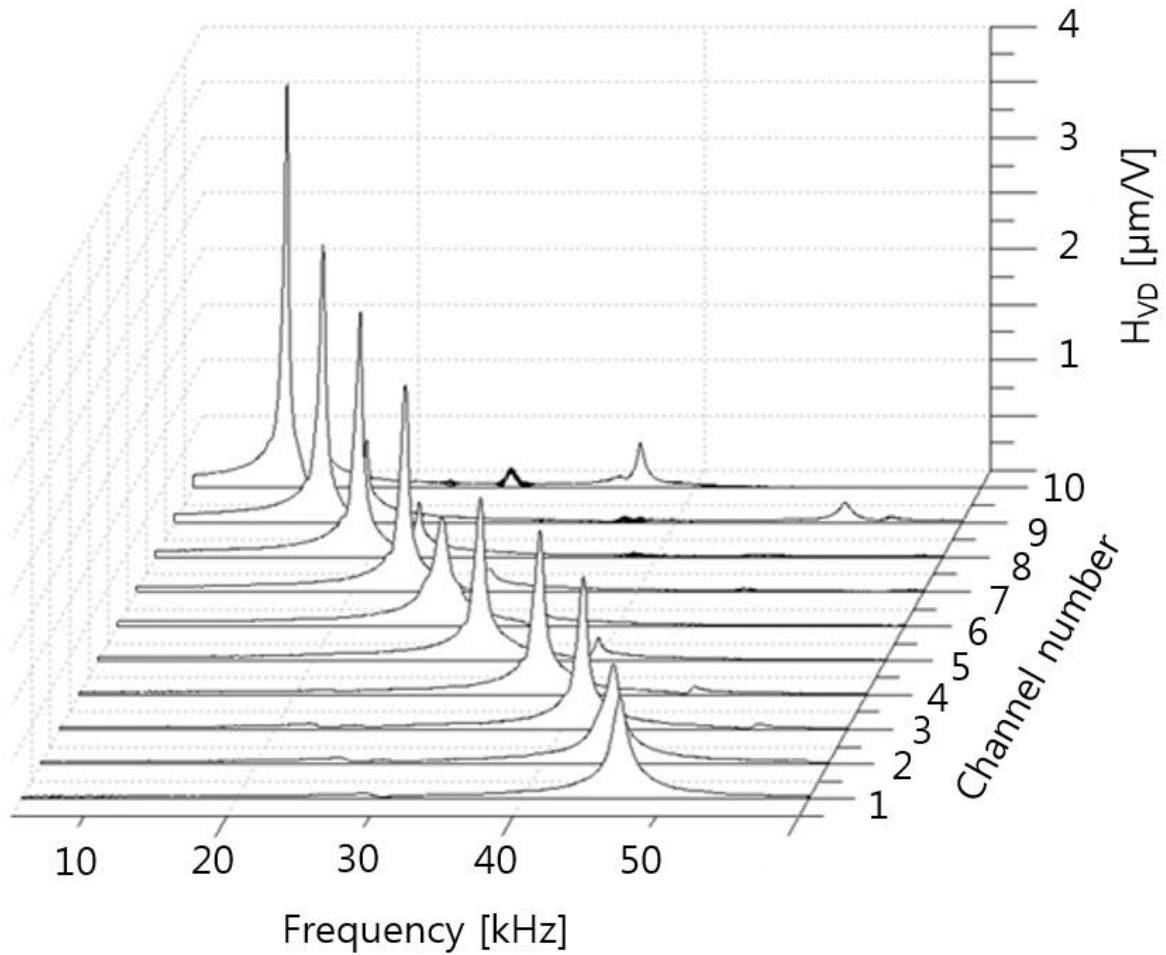
Figure 4.3 Electro-mechanical transfer function (H$_{VD}$) for sample ABM-A 02 in air.

4.1.2 Piezoelectric responses of the ABM

Figure 4.4 shows the measured piezoelectric response from channel 4 to channel 10 in sample ABM-A 02. Measurement of piezoelectric response was conducted using 7 beams due to the limitation of a loudspeaker in air. Its voltage level is pretty low, in the range 2 - 5 µV at the resonance frequencies. However, the WSBA generated the piezoelectric outputs to identify the resonance frequency of each beam. The piezoelectric voltage output from the NSBA is shown in figure 4.4 (b). The measured piezoelectric signal was like noise level caused by the narrow supports, small strain in the piezoelectric beams, and rigid-body motion [36].
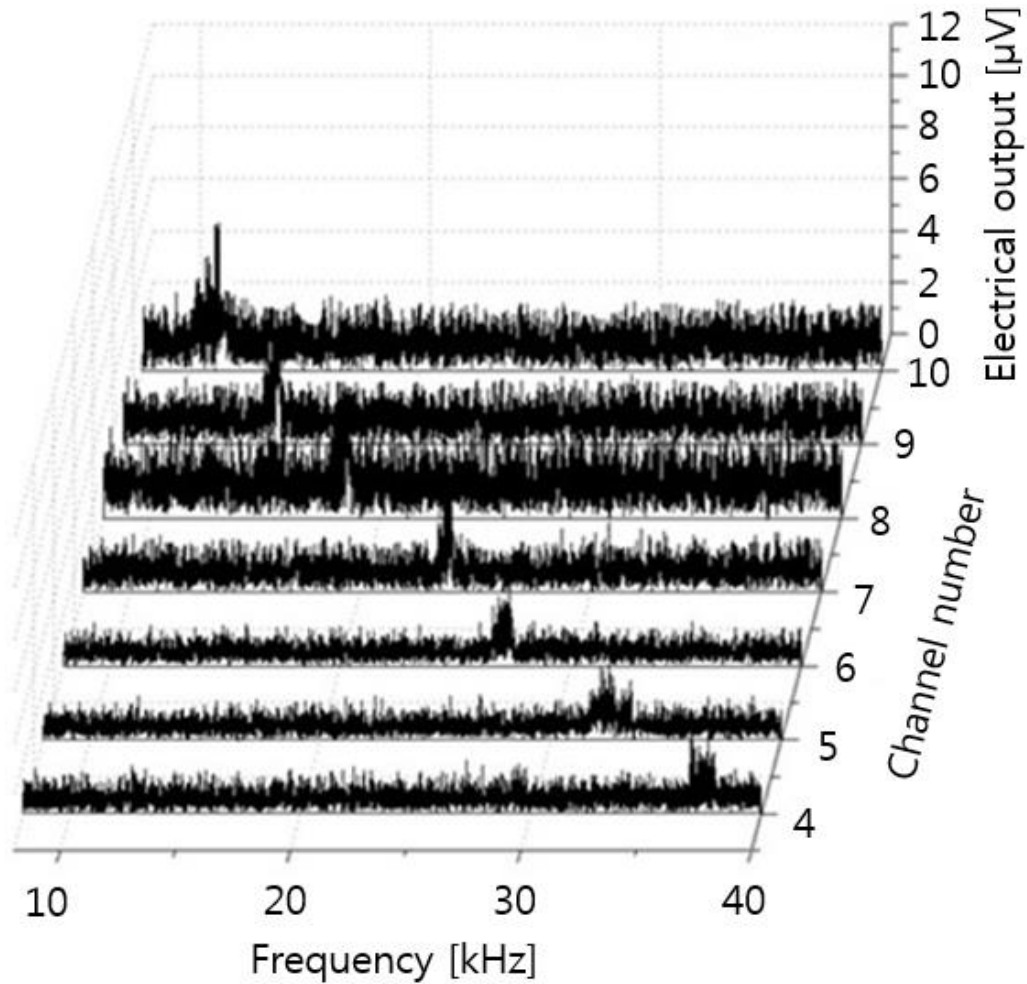

(a)
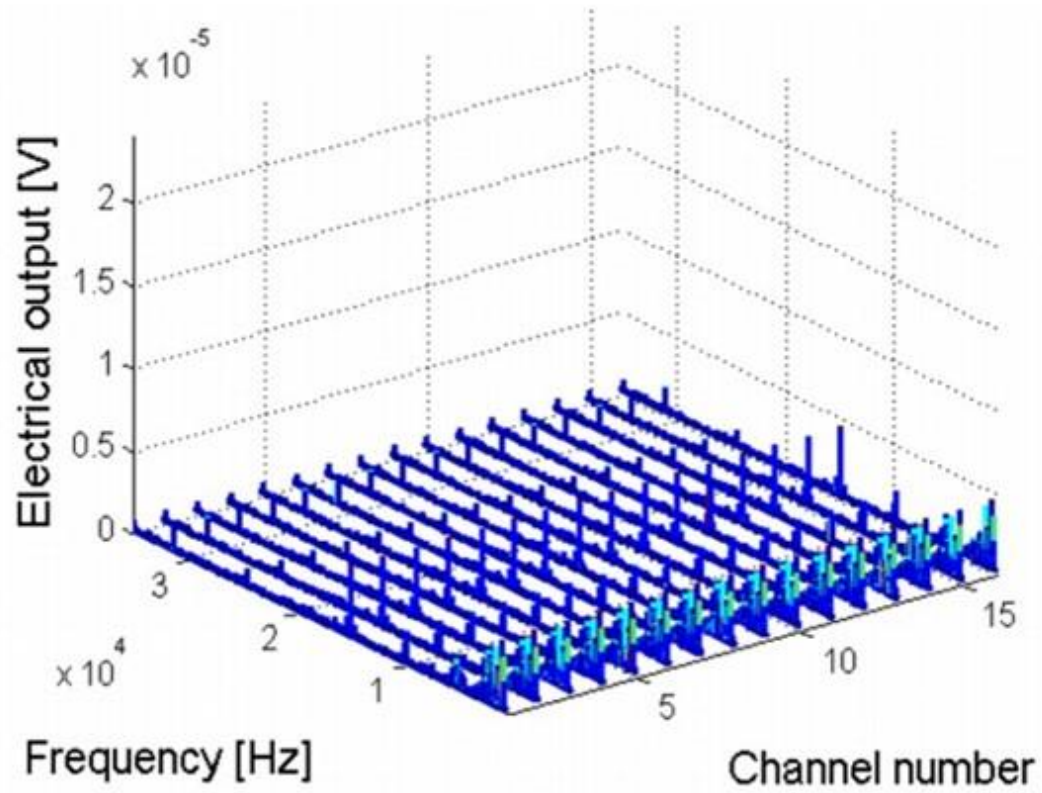
(b)

Figure 4.4 Piezoelectric voltage output of the beams measured by acoustic stimulus in air: (a) the WSBA and, (b) the NSBA [6, 36].

Figure 4.5 (a), (b) show the piezoelectric response of the 8th channel in the advanced ABM beam array for sample ABM-A 02. The piezoelectric output voltage during acoustic stimulus was 390 µV in time domain, as shown in figure 4.5 (a). The input acoustic stimulus is shown in the upper right corner. Figure 4.5 (b) shows the electrical signal strength of 4.8 µV in frequency domain. The input acoustic stimulus is shown in the upper right corner.
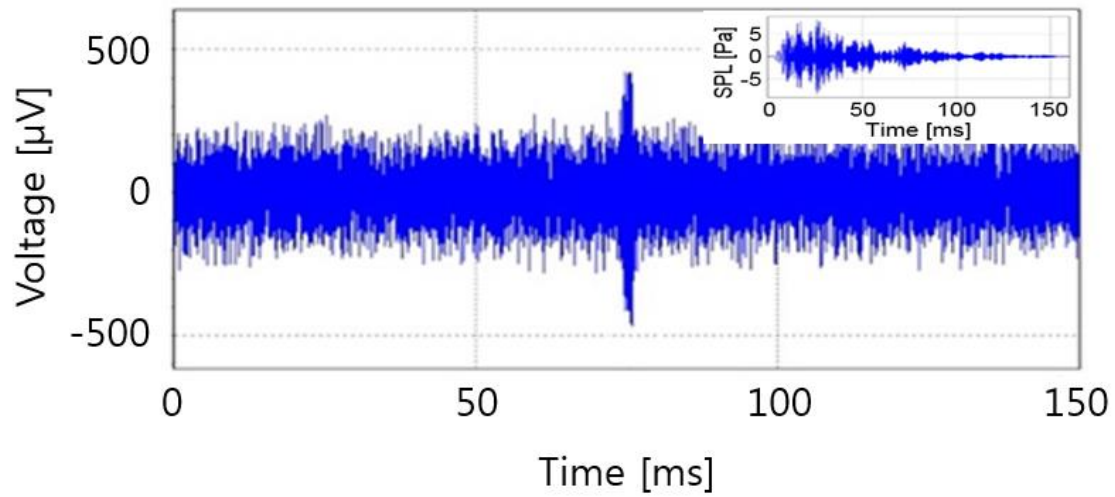

(a)
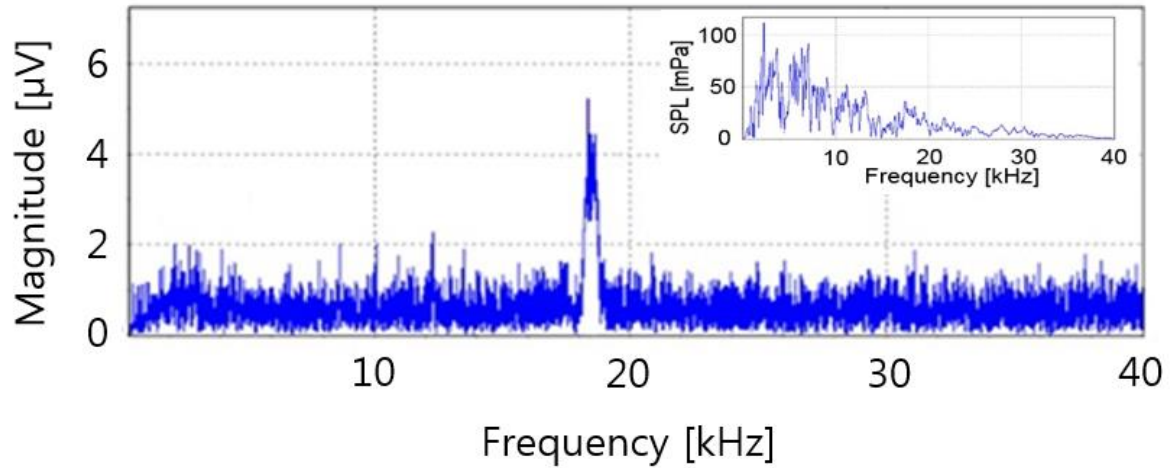
(b)

Figure 4.5 Piezoelectric response of the 8th channel in the advanced ABM beam array for sample ABM-A 02: (a) Piezoelectric voltage output in time domain and input acoustic stimulus, and (b) Piezoelectric voltage output in frequency domain and input acoustic stimulus.

Figure 4.6 is shown three grapes of the resonance frequencies at the point of showing the displacement and piezoelectric voltage during acoustic or electric stimulus. The standard deviation expressed in error bars. From this grape, we can know that the resonance frequencies of each beam systematically shifted as the beam length increased (i.e., with increasing channel number), with resonance frequencies in the range 10.5–36.5 kHz (for acoustic stimulus) or 11.1-47.7 kHz (for electric stimulus). Furthermore, the frequencies of three grapes in the range 10.5–36.5 kHz were corresponded with each other. From these results, we can know that three types of measurement results have high reliability and the fabricated ABM had a function which is acoustic-to-electric energy conversion.
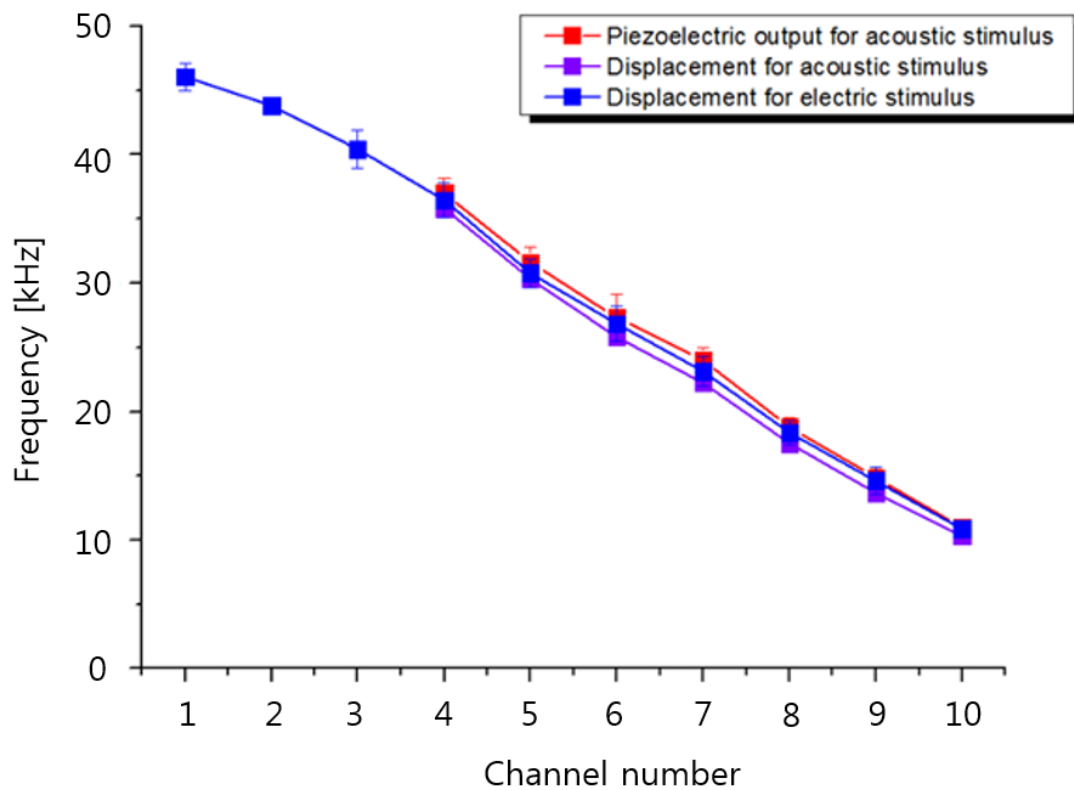

Figure 4.6 Resonance frequencies at the point of showing the displacement and piezoelectric voltage during acoustic or electric stimulus.

4.2 Performance characteristics of the ABM in fluid

4.2.1 Mechanical responses of the ABM

The acoustic stimulus in the range of 100 Hz - 20 kHz was applied using a loudspeaker to identify the displacement per each channel in fluid. Figure 4.7 shows the displacement from channel 1 to channel 10 of sample ABM-A 02 measured by acoustic stimulus. However, the magnitudes of displacement measured in fluid were similar or large in comparison to them of displacement measured in air. Furthermore, the frequency separation of beam was not well in fluid. From these results, we determined that the acoustic stimulus in air does not travel in fluid well. The acoustic stimulus applied using a loudspeaker made the vibration in fluid. The vibration of water had an effect on the displacement of beam. As a result, the accurate results were not obtained.
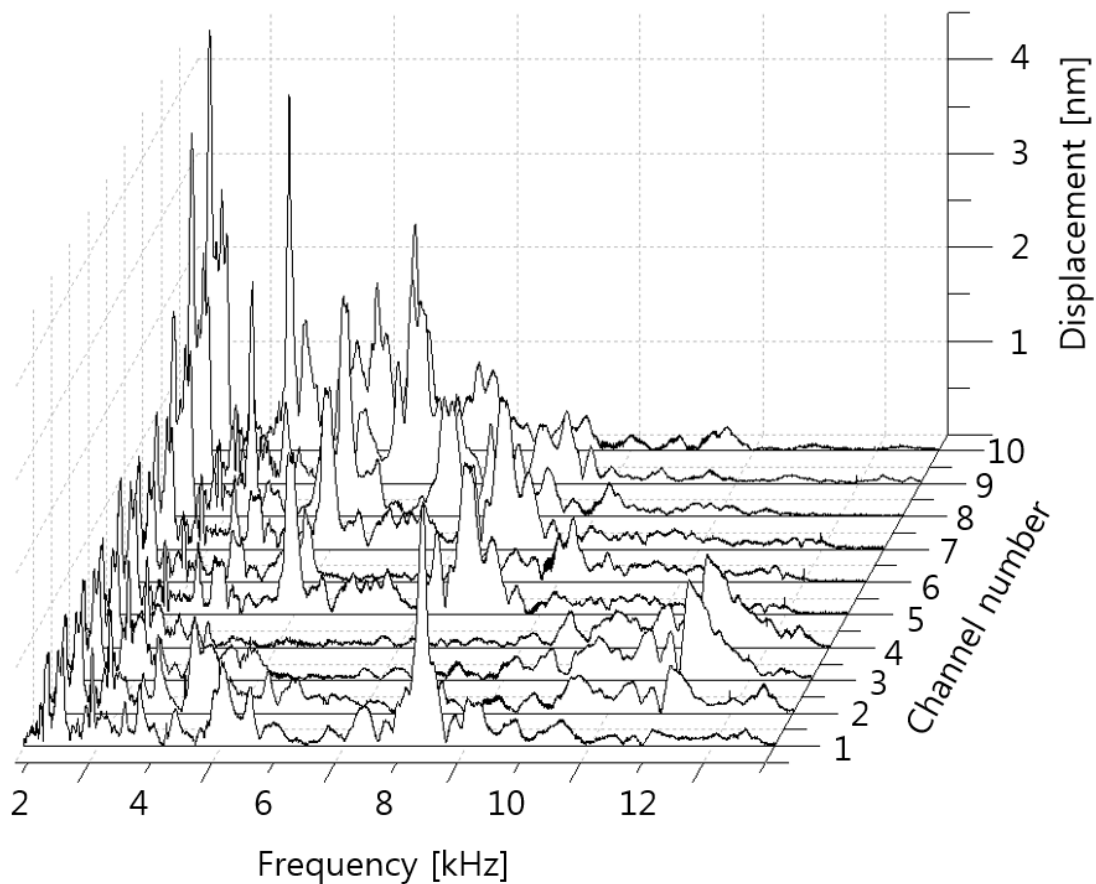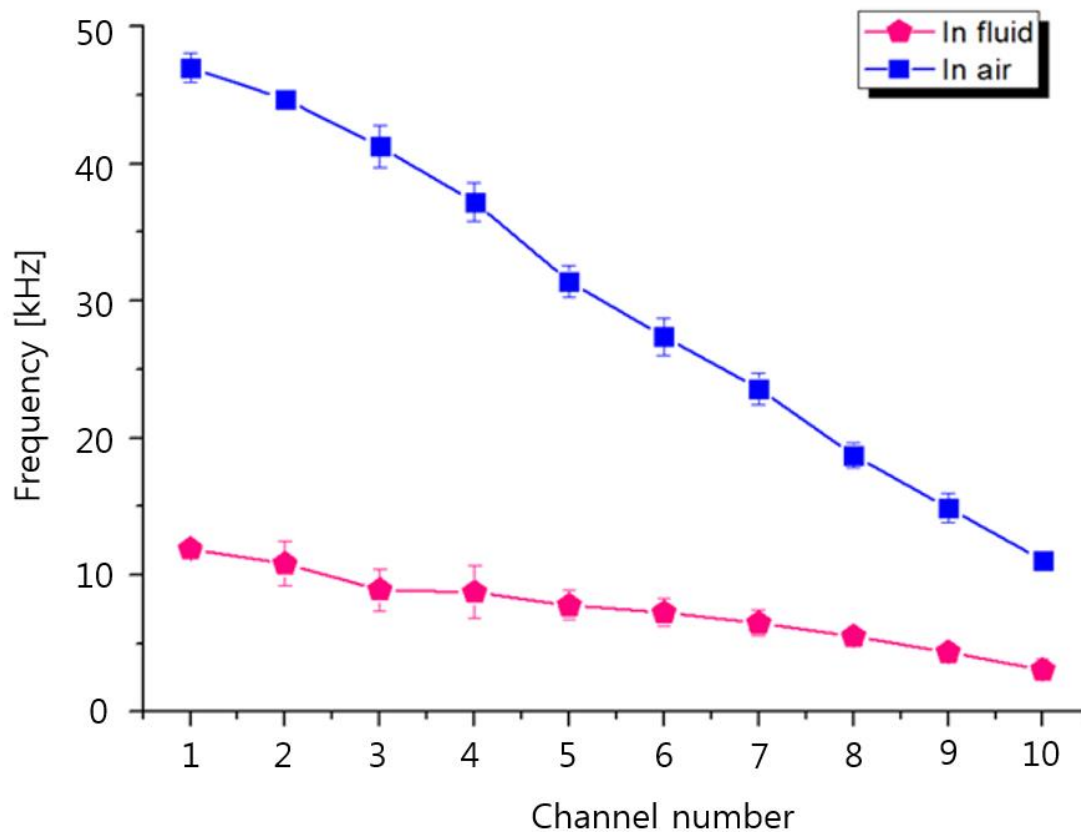

Figure 4.7 Displacement of the beams in the array for sample ABM-A 02 during acoustic stimulus in fluid

To determine the vibrating characteristics of the ABM in fluid, the electric stimulus of AC with 1V was applied by two probe tips, which were located in top and bottom electrode of the ABM. Table 4.2 shows the mean resonance frequencies per each beam length during electric stimulus in air and fluid. The measured mean frequencies of the ABM in air were in the range 11.1 - 47.7 kHz, whereas the measured mean frequencies of the ABM in fluid were in the range 3.1 - 11.9 kHz.

Table 4.2 Mean resonance frequencies per each beam length in three samples for electric stimulus in air and fluid.

Channel number	Beam length (μm)	Electric stimulus tests in air	Electric stimulus tests in fluid
		Mean resonance frequency [kHz]	Mean resonance frequency [kHz]
1	1306	47.648	11.883
2	1338	44.703	10.824
3	1423	41.235	8.917
4	1516	37.193	8.728
5	1668	31.385	7.789
6	1818	27.380	7.264
7	1994	23.588	6.495
8	2323	18.719	5.520
9	2673	14.891	4.373
10	3194	11.078	3.084

Figure 4.7 shows a grape showing mean resonance frequencies of three samples (ABM-A 02, ABM-A 08, and ABM-A 09) with respect to the channel number during electric stimulus in fluid. For clear comparison of frequency shift in air and fluid environment, figure 4.7 also shows a grape showing mean resonance frequencies of three samples with respect to the channel number during electric stimulus in air. The standard deviation expressed in error bars. In fluid, the resonance frequencies dropped by one forth, which are within the audible frequency range (i.e., 20 Hz – 20 kHz). This frequency shift in fluid environment is caused by the viscous-damping effect of water [29].


Figure 4.8 Mean resonance frequencies for three samples (ABM-A 02, ABM-A 08, and ABM-A 09) during electric stimulus in air and fluid.

Figure 4.8 shows the displacement of the beams for sample ABM-A 08 during electric stimulus in fluid. The maximum displacement of the beams for electric stimulus was in the range 0.5 - 3 nm shown in figure 4.8. The displacement in fluid decreased as compared with the displacement in air caused by the viscous-damping effect of water. The wave was damped in the high viscous one [29]. However, the displacement peaks were very clear compared with some experimental results in fluid (i.e., they measured the displacement of the membrane type ABM in fluid) [9, 29]. The result is because of the great frequency selectivity of a beam array type ABM [33].
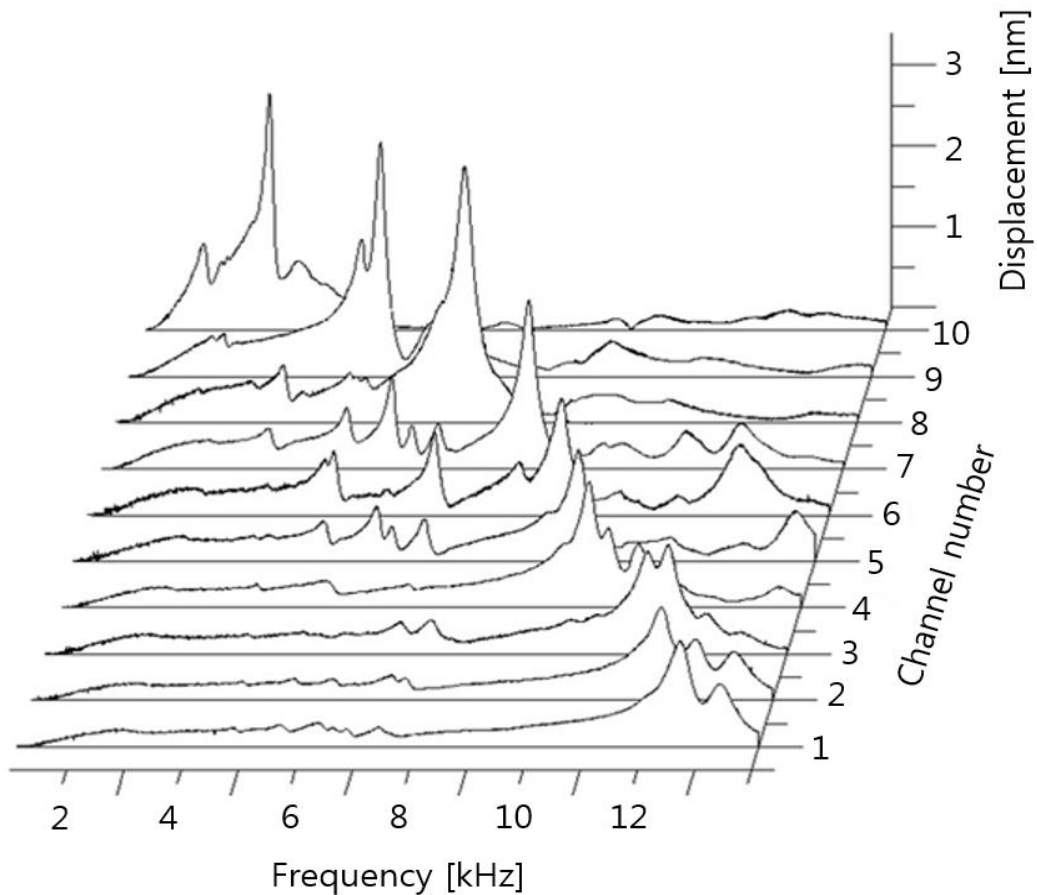
Figure 4.9 Displacement of the beams in the array for sample ABM-A 08 during electric stimulus in fluid.

In the basis of the displacement for sample ABM-A 08 during electric stimulus in fluid, an electro-mechanical transfer function (H_{VD}) was normalized by the applied voltage. (i.e., an acoustic-mechanical transfer function (H_{PD}) was excepted by incorrect acoustic stimulus measured using microphone.) Figure 4.9 shows an electro-mechanical transfer function (H_{VD}) for sample ABM-A 08 in fluid. The maximum magnitude of the transfer function for electric stimulus was in the range $0.07 - 0.28$ µm/V. From the transfer function in figure 4.9, we identified the resonance frequencies corresponding to the first bending mode of the beams in fluid once again.
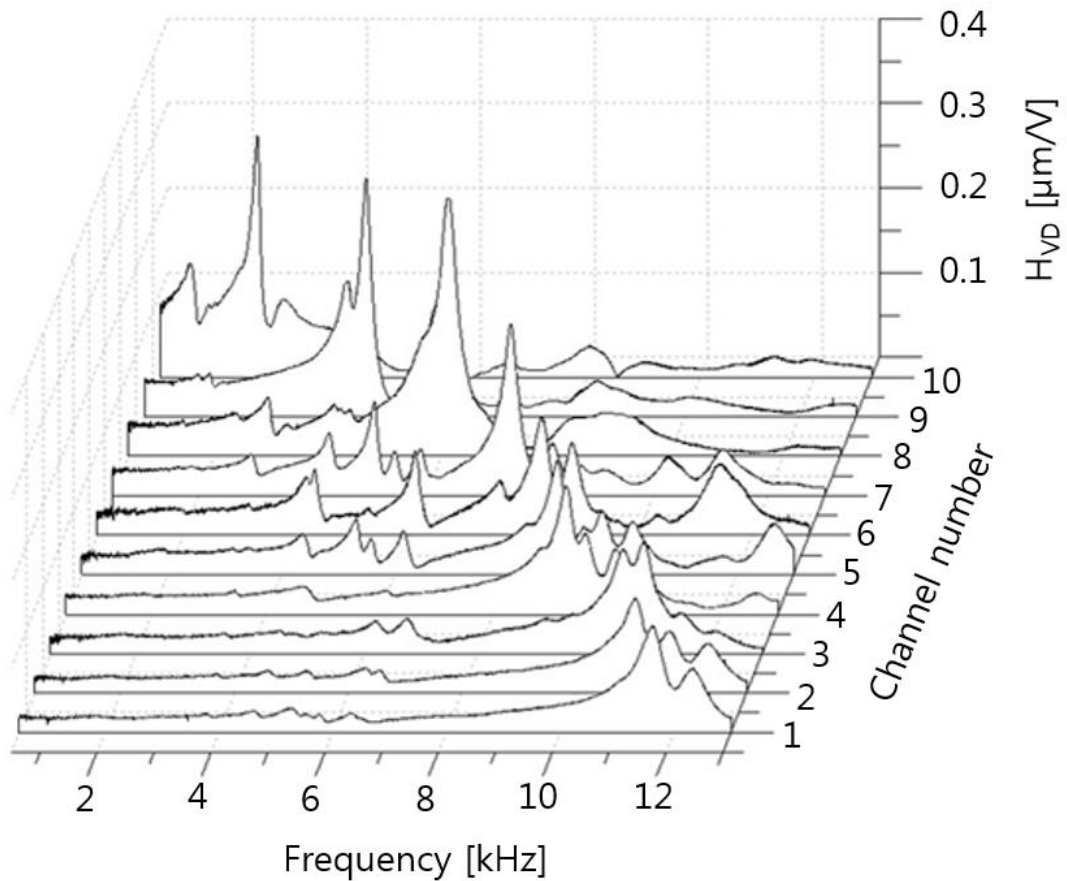
Figure 4.10 Electro-mechanical transfer function (H_{VD}) for sample ABM-A 08 in fluid.

4.2.2 Piezoelectric responses of the ABM

      Figure 4.11 shows the piezoelectric voltage outputs of 10 channels measured during acoustic stimulus in fluid. Figure 4.12 shows the piezoelectric responses of the 8th channel for sample ABM-A 02 in time and frequency domain. The piezoelectric voltage outputs in the range of $5 - 28$ µV were measured during acoustic stimulus. However, the magnitudes of piezoelectric voltage measured in fluid were large in comparison to them of piezoelectric voltage measured in air. The frequency separation of beam was not well in fluid. The cause of these results was that the acoustic stimulus in air does not travel in fluid well.
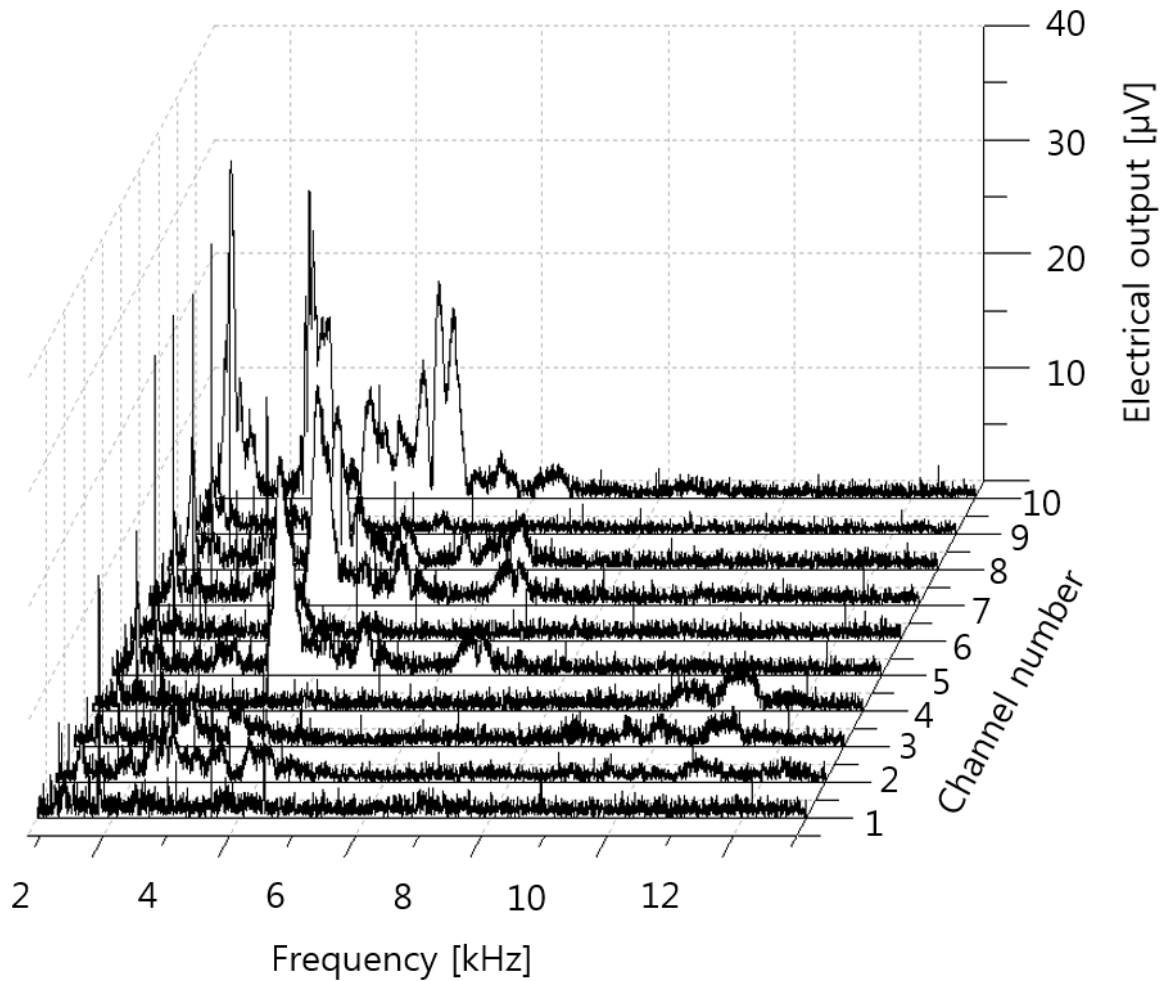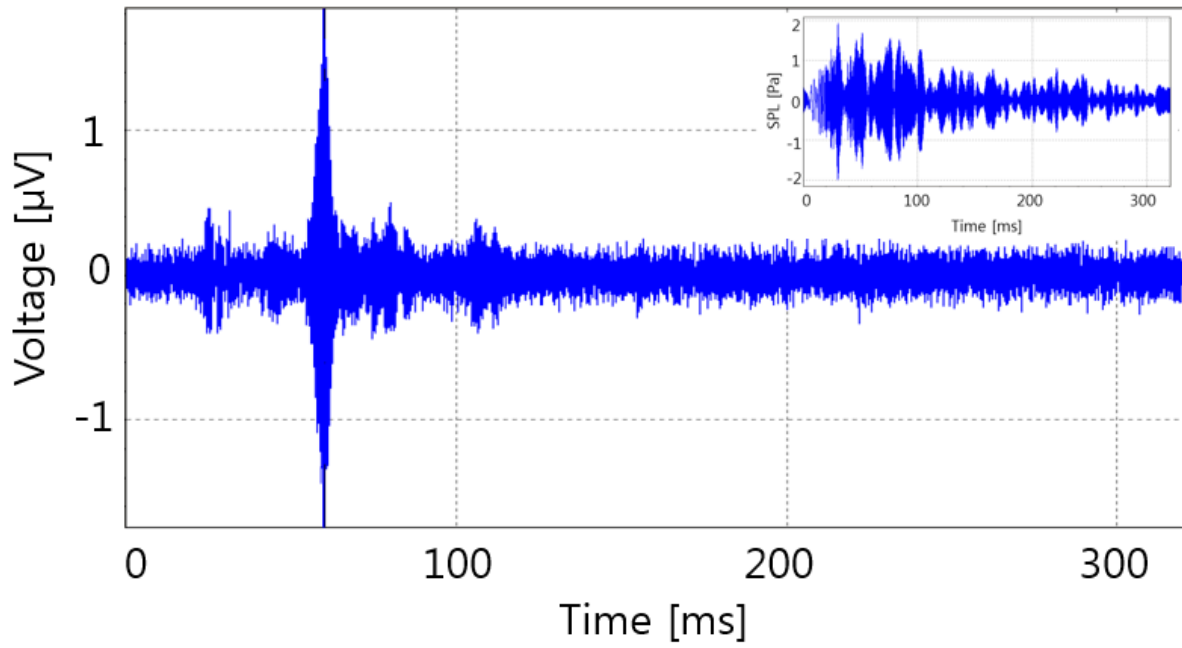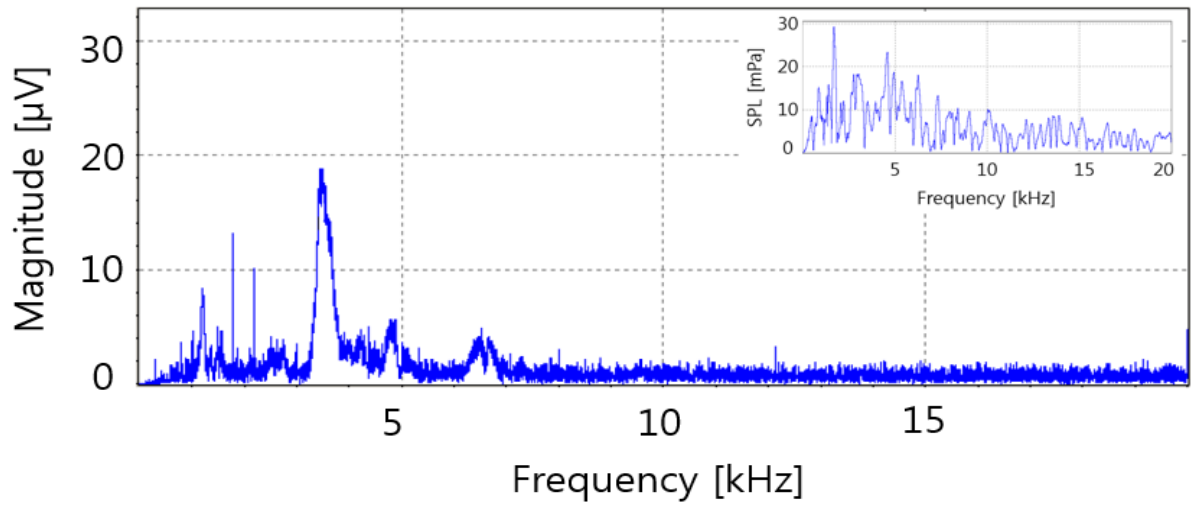

Figure 4.11 Piezoelectric voltage output of the beams measured by acoustic stimulus in fluid.

(a)

(b)

Figure 4.12 Piezoelectric response of the 8th channel in the advanced ABM beam array for sample ABM-A 02 in fluid: (a) Piezoelectric voltage output in time domain and input acoustic stimulus, and (b) Piezoelectric voltage output in frequency domain and input acoustic stimulus.

4.3 Discussions

The advanced ABM showed the mechanical displacement and piezoelectric voltage output at the resonance frequencies. In comparison with the NSBA, the piezoelectric voltage output of the WSBA was measured in the range 2 - 5 µV at the resonance frequencies, whereas the piezoelectric voltage output of the NSBA was very week as much as noise level. However, the measured frequencies of the WSBA were in the range 11.1 - 47.7 kHz (i.e., the measured frequencies during acoustic stimulus assume nearly to correspond with the measured frequencies during electric stimulus.). This frequency range was higher than the audible frequency range (i.e., 20 Hz - 20 kHz). It was difficult exactly to control the etched dimensions of silicon under the beams for XeF_2 etching process. The beam lengths were reduced compared with the calculated lengths. Also, the residual stresses existing in the beams was improved by deposition LPCVD Si_3N_4 in comparison with NSBA, but a few residual stresses still existed [36]. For these reasons, the measured frequency range was higher than the theoretical frequency range. The optimized processing condition in XeF_2 etching process and the improvement of the residual stress are expected to manufacture a device which has the audible frequency range during acoustic and electric stimulus in air.

We confirmed that the measured frequencies for electric stimulus in fluid were in the audible frequency range (i.e., 3.1 - 11.9 kHz) because of the frequency shift caused by viscous-damping effect of water. The displacement peaks at the resonance frequencies were very clear compared with these ABMs of Shintaku and White and Grosh *et al.*(i.e., they measured the displacement of their membrane type ABMs using fluidic chamber in fluid) [9, 29]. Because the frequency selectivity of a beam array type ABM is better than membrane type ABM's frequency selectivity as shown in our previous research [33]. However, the displacement peaks for acoustic stimulus in fluid were not clear. The

frequency separation was not well. Because the acoustic stimulus in air does not travel in fluid well. To obtain clear frequency selectivity for acoustic stimulus, the input stimulus using underwater vibration system is needed. Also, the experiment in fluid was only conducted using DI water. The density and the viscosity of the lymph fluid in cochlea are reported as $1.0 * 10^3 \text{ kg/m}^3$ and from $1.0 * 10^{-3}$ to $1.97 * 10^{-3}\text{Pa s}$, respectively [31, 50, 51]. The experiment in fluid using silicon oil, which is similar to the density and the viscosity of lymph fluid, is expected to rise the reliability of the measurement results.

5. CONCLUSIONS

We fabricated an the advanced MEMS artificial basilar membrane using XeF_2 etching, which are cheap and simple process for silicon etching compared with DRIE reported in Ref [10]. To remove the narrow supports in ABM of Kim et al. is redesigned as changing the dimension of open area: the gap both electrodes and open area is widened about 100 μm. Also, the deformation of beams was minimized by controlling the residual stress: a tensile stressed LPCVD Si_3N_4 was deposited on SiO_2 layer to compensate for the compressive stress of a SiO_2.

AlN beam array of ABM were composed of 10 beams, each beam had different length for frequency separation. In the experiments, the mechanical responses of beams were measured using SLDV for acoustic or electric stimulus. Each beam was excited by acoustic or electric waveforms of periodic chirp generated from the SLDV control module. Especially, acoustic stimulus tests were conducted from channel 4 to channel 10 by limitation of a loudspeaker: it is possible to measure the beams which have the resonance frequencies under 40kHz. The measured resonance frequencies of each beam systematically shifted as the beam length increased, with resonance frequencies in the range 10.5 - 36.5 kHz (acoustic stimulus) or 11.1 - 47.7 kHz (electric stimulus). The maximum displacement of the beams for was in the range 0.5 - 3.2 nm (acoustic stimulus) or 10 - 40 nm (electric stimulus). The displacement peaks shifted toward lower frequencies as the beam length increased. The piezoelectric voltage output was measured using acoustic stimulus. Although the measured piezoelectric voltage had some noise, but it was in the range 2 - 5 µV at the resonance frequencies. In fluid environment, we measured the displacement of the ABM at the resonance frequencies using electric stimulus. From the viscous-damping effect of water, the resonance frequency dropped in the range of 3.1 - 11.9 kHz (i.e., within audible frequency range). The magnitude of displacement decreased in

fluid than in air. However, the displacement peaks were very clear compared with some researches using the membrane type ABM.

Therefore, the device was applicable as substitute of the conventional CI to mimic the functions of cochlea. The potential as fully implantable device was identified through performance characteristics of the ABM in air and fluid.

REFERENCES

[1]   F.-G. Zeng, S. Rebscher, W. Harrison, X. Sun, and H. Feng, "Cochlear implants: system design, integration, and evaluation," *Biomedical Engineering, IEEE Reviews in,* vol. 1, pp. 115-142, 2008.

[2]   R. Nobili, F. Mammano, and J. Ashmore, "How well do we understand the cochlea?," *Trends in neurosciences,* vol. 21, pp. 159-167, 1998.

[3]   J. Rauschecker and R. Shannon, "Sending sound to the brain," *Science,* vol. 295, pp. 1025-1029, 2002.

[4]   V. J. Molfese, A. Prokasky, K. M. Rudasill, I. H. Acar, X. Tu, K. Sirota*, et al.*, "Prenatal Development: Annotated Bibliography," 2013.

[5]   K. S. Saladin and L. Miller, *Anatomy & physiology*: McGraw-Hill, 1998.

[6]   W. J. Song, J. Jang, S. Kim, and H. Choi, "Piezoelectric performance of continuous beam and narrow supported beam arrays for artificial basilar membranes," *Electronic Materials Letters,* vol. 10, pp. 1011-1018, 2014.

[7]   L. Robles and M. A. Ruggero, "Mechanics of the mammalian cochlea," *Physiological reviews,* vol. 81, pp. 1305-1352, 2001.

[8]   P. Dallos, "Overview: cochlear neurobiology," in *The cochlea*, ed: Springer, 1996, pp. 1-43.

[9]   R. D. White and K. Grosh, "Microengineered hydromechanical cochlear model," *Proceedings of the National Academy of Sciences of the United States of America,* vol. 102, pp. 1296-1301, 2005.

[10]   R. R. GACEK, "Neurobiology of Hearing: The Cochlea," *Archives of Otolaryngology—Head & Neck Surgery,* vol. 113, p. 671, 1987.

[11]   A. Salt, "The cochlear fluids: perilymph and endolymph," *Neurobiology of hearing: the cochlea,* pp. 109-122, 1986.

[12]   G. von Békésy, "Travelling waves as frequency analysers in the cochlea," *Nature,* vol. 225, pp. 1207-1209, 1970.

[13]   R. Patuzzi, "Cochlear micromechanics and macromechanics," in *The cochlea*, ed: Springer, 1996, pp. 186-257.

[14]   T. Ren, "Longitudinal pattern of basilar membrane vibration in the sensitive cochlea," *Proceedings of the National Academy of Sciences,* vol. 99, pp. 17101-17106, 2002.

[15]   C.-P. Richter, B. N. Evans, R. Edge, and P. Dallos, "Basilar membrane vibration in the gerbil hemicochlea," *Journal of neurophysiology,* vol. 79, pp. 2255-2264, 1998.

[16]   C. D. Geisler, *From sound to synapse: physiology of the mammalian ear*: oxford university press, 1998.

[17]   A. F. Ryan, "Protection of auditory receptors and neurons: evidence for interactive damage," *Proceedings of the National Academy of Sciences,* vol. 97, pp. 6939-6940, 2000.

[18]   P. C. Loizou, "Introduction to cochlear implants," *Engineering in Medicine and Biology Magazine, IEEE,* vol. 18, pp. 32-42, 1999.

[19]   G. E. Loeb, "Cochlear prosthetics," *Annual review of neuroscience,* vol. 13, pp. 357-371, 1990.

[20]   J. T. Rubinstein and C. A. Miller, "How do cochlear prostheses work?," *Current Opinion in Neurobiology,* vol. 9, pp. 399-404, 1999.

[21]   B. C. Papsin and K. A. Gordon, "Cochlear implants for children with severe-to-profound hearing loss," *New England Journal of Medicine,* vol. 357, pp. 2380-2387, 2007.

[22] K. Nie, A. Barco, and F.-G. Zeng, "Spectral and temporal cues in cochlear implant speech perception," *Ear and hearing,* vol. 27, pp. 208-217, 2006.

[23] S. B. Waltzman, "Cochlear implants: current status," *Expert Review of Medical Devices,* vol. 3, pp. 647-655, 2006.

[24] G. Von Békésy, "Current status of theories of hearing,," *Science,* vol. 123, pp. 779-783, 1956.

[25] G. Von Békésy, "Hearing theories and complex sounds," *The Journal of the Acoustical Society of America,* vol. 35, pp. 588-601, 1963.

[26] I. Avramidou, N. Dillier, W.-K. Lai, and J. Vörös, "Excitability Controlled Coding (ECC): Real Time Implementation."

[27] J. Jang, S. Kim, D. J. Sly, S. J. O'leary, and H. Choi, "MEMS piezoelectric artificial basilar membrane with passive frequency selectivity for short pulse width signal modulation," *Sensors and Actuators A: Physical,* vol. 203, pp. 6-10, 2013.

[28] B. S. Wilson and M. F. Dorman, "Cochlear implants: a remarkable past and a brilliant future," *Hearing research,* vol. 242, pp. 3-21, 2008.

[29] H. Shintaku, T. Nakagawa, D. Kitagawa, H. Tanujaya, S. Kawano, and J. Ito, "Development of piezoelectric acoustic sensor with frequency selectivity for artificial cochlea," *Sensors and Actuators A: Physical,* vol. 158, pp. 183-192, 2010.

[30] F. Chen, H. I. Cohen, T. G. Bifano, J. Castle, J. Fortin, C. Kapusta, *et al.*, "A hydromechanical biomimetic cochlea: Experiments and models," *The Journal of the Acoustical Society of America,* vol. 119, pp. 394-405, 2006.

[31] G. Zhou, L. Bintz, D. Z. Anderson, and K. E. Bright, "A life-sized physical model of the human cochlea with optical holographic readout," *The Journal of the Acoustical Society of America,* vol. 93, pp. 1516-1523, 1993.

[32] M. J. Wittbrodt, C. R. Steele, and S. Puria, "Developing a physical model of the human cochlea using microfabrication methods," *Audiology and Neurotology,* vol. 11, pp. 104-112, 2006.

[33] W. J. Song, J. Jang, S. Kim, and H. Choi, "Influence of mechanical coupling by SiO2 membrane on the frequency selectivity of microfabricated beam arrays for artificial basilar membranes," *Journal of Mechanical Science and Technology,* vol. 29, pp. 963-971, 2015.

[34] K. Tanaka, M. Abe, and S. Ando, "A novel mechanical cochlea "Fishbone" with dual sensor/actuator characteristics," *Mechatronics, IEEE/ASME Transactions on,* vol. 3, pp. 98-105, 1998.

[35] T. Xu, M. Bachman, F.-G. Zeng, and G.-P. Li, "Polymeric micro-cantilever array for auditory front-end processing," *Sensors and Actuators A: Physical,* vol. 114, pp. 176-182, 2004.

[36] S. Kim, W. J. Song, J. Jang, J. H. Jang, and H. Choi, "Mechanical frequency selectivity of an artificial basilar membrane using a beam array with narrow supports," *Journal of Micromechanics and Microengineering,* vol. 23, p. 095018, 2013.

[37] J. Jang, J. Lee, S. Woo, D. J. Sly, L. J. Campbell, J.-H. Cho, *et al.*, "A microelectromechanical system artificial basilar membrane based on a piezoelectric cantilever array and its characterization using an animal model," *Scientific reports,* vol. 5, 2015.

[38] H. S. Lee, J. Chung, G. T. Hwang, C. K. Jeong, Y. Jung, J. H. Kwak, *et al.*, "Flexible Inorganic Piezoelectric Acoustic Nanosensors for Biomimetic Artificial Hair Cells," *Advanced Functional Materials,* vol. 24, pp. 6914-6921, 2014.

[39] M. Hara, J. Kuypers, T. Abe, and M. Esashi, "Surface micromachined AlN thin film 2GHz resonator for CMOS integration," *Sensors and Actuators A: Physical,* vol. 117, pp. 211-216, 2005.

[40] P. Abgrall and N.-T. Nguyen, *Nanofluidics*: Artech House, 2014.

[41] D. G. Hwang, Y. M. Chae, K. S. Hwang, J. Y. Kang, and S. H. Lee, "Fabrication and characterization of PZT (lead zirconate titanate) bridge-shaped resonator for mass sensing application," *Journal of electroceramics,* vol. 29, pp. 225-234, 2012.

[42] H. Shintaku, T. Kobayashi, K. Zusho, H. Kotera, and S. Kawano, "Wide-range frequency selectivity in an acoustic sensor fabricated using a microbeam array with non-uniform thickness," *Journal of Micromechanics and Microengineering,* vol. 23, p. 115014, 2013.

[43] B. V. Krishna, S. Bose, and A. Bandyopadhyay, "Low stiffness porous Ti structures for load-bearing implants," *Acta biomaterialia,* vol. 3, pp. 997-1006, 2007.

[44] H. Choi, J. Ding, A. Bandyopadhyay, M. Anderson, and S. Bose, "Characterization and modeling of a piezoelectric micromachined ultrasonic transducer with a very large length/width aspect ratio," *Journal of micromechanics and microengineering,* vol. 18, p. 025037, 2008.

[45] S.-J. Chen, Y. Choe, L. Baumgartel, A. Lin, and E. S. Kim, "Edge-released, piezoelectric MEMS acoustic transducers in array configuration," *Journal of Micromechanics and Microengineering,* vol. 22, p. 025005, 2012.

[46] T. Wang and C. Lee, "Zero-Bending Piezoelectric Micromachined Ultrasonic Transducer (pMUT) With Enhanced Transmitting Performance."

[47] W.-H. Chuang, T. Luger, R. K. Fettig, and R. Ghodssi, "Mechanical property characterization of LPCVD silicon nitride thin films at cryogenic temperatures," *Microelectromechanical Systems, Journal of,* vol. 13, pp. 870-879, 2004.

[48] T. Obikawa and E. Usui, "Computational machining of titanium alloy—finite element modeling and a few results," *Journal of Manufacturing Science and Engineering,* vol. 118, pp. 208-215, 1996.

[49] M. Kashiwagi, S. Hirata, K. Harada, Y. Zheng, K. Miyazaki, M. Yahiro*, et al.*, "Enhanced figure of merit of a porous thin film of bismuth antimony telluride," 2011.

[50] J. D. Bronzino, "Principles of electroencephalography," *The Biomedical Engineering Handbook,* vol. 1, 1995.

[51] J. Ten Kate and J. Kuiper, "The viscosity of the pike's endolymph," *Journal of Experimental Biology,* vol. 53, pp. 495-500, 1970.

요 약 문

제논 에칭을 이용하여 제작된 개선된 MEMS 인공 기저막의 공기와

유체에서의 특성 평가.

인공 와우는 선천적 또는 후천적으로 달팽이관의 유모세포의 손상으로 인해 완전히 청력을 손실한 환자들의 청력 회복을 위한 인체 삽입 형 전자기기이다. 비록 상용화된 인공 와우가 많은 성공을 거두어 왔지만, 외부장치로 인한 장애의 노출, 높은 배터리 소모, 잦은 충전 및 복잡한 신호 처리 회로 등의 여러 한계점을 가지고 있다. 이러한 한계점을 극복하기 위해 현재 MEMS 기술을 이용한 체내 완전 삽입형 인공 기저막에 대한 연구가 활발히 진행되고 있다. 인공 기저막은 주파수 분리와 전기 · 기계적 변환과 같은 달팽이관의 기능을 모사한 MEMS 디바이스이다. 우리 그룹의 이전 연구에서는 제논 에칭을 이용한 빔 어레이 타입의 주파수 분리 기능을 가지는 인공 기저막을 제작하였고 그 성능을 평가하였다. 하지만 공정과정 중에 생긴 narrow supports 에 의한 빔의 변형 및 압전 신호의 측정불가라는 한계점을 가지게 되었다. 그리하여, 인공 기저막의 압전 신호를 향상시키기 위한 방안으로 DRIE 공정을 이용한 인공 기저막을 제작하였고, 특성 평가를 통해 뚜렷한 주파수 분리 및 압전 신호 발생을 입증 하였다. 그러나, DRIE 공정으로 제작된 인공 기저막은 제작 비용이 많이 들고, 공정 과정이 복잡하다는 한계점을 가지고 있다.

본 연구에서는 앞서 연구한 두 가지의 타입의 인공 기저막의 한계점을 개선하기 위하여 제논 에칭을 이용한 개선된 MEMS 압전 인공 기저막을 제작하였다. 제논 에칭은 DRIE 공정에 비해 공정과정이 매우 간단하고 비교적 공정비가 낮다는 장점을 가지고 있어 사용되었다. 더불어, 잔류응력에 의해 발생되는 빔의 측면 변형을 줄이기 위해 LPCVD Si_3N_4 를 증착하였다. 마지막으로, 빔의 rigid body motion 을 개선하기 위해 narrow supports 를 가지지 않는 연속적인 빔 구조로 디자인 되었다.

각 빔의 공진 주파수와 압전 신호는 소리 및 전기 신호 입력을 인가한 후 SLDV 를 이용하여 측정되었다. 소리 자극 시, 제작된 인공 기저막은 10 개의 채널 중 7 개의 채널에서

10.5 – 36.5 kHz 범위의 공진 주파수와 2 – 5 µV 의 압전 신호를 보였다. 전기 자극 시, 제작된 인공 기저막은 10 개의 채널에서 11.1 – 47.7 kHz 범위의 공진 주파수를 보였다. 또한, 체내 삽입형 디바이스로의 가능성을 확인하기 위해 인공 기저막의 진동 특성을 유체 환경에서 평가하였다. 전기 자극 후 디바이스의 주파수와 변위 특성을 평가해 본 결과, 물의 점성 감쇠 효과에 의해 공기 중에서 11.1 – 47.7 kHz 이었던 주파수 범위가 유체 내에서 3.1 – 11.9 kHz 의 가청 주파수 범위로 떨어졌다. 빔이 진동되는 크기는 공기 중에서 10 – 40 ㎚ 이었던 변위가 유체 내에서 0.5 – 3 ㎚ 의 변위로 감소하였으나 여전히 뚜렷한 주파수 분리를 보임을 확인하였다.

　　이러한 결과를 통해, 제작된 인공 기저막이 주파수 분리와 전기·기계적 변환과 같은 달팽이관의 기능을 모사함을 확인하였고, 유체 환경에서의 특성 평가를 통해 완전 삽입형 디바이스로서의 가능성을 확인하였다.

핵심어: 인공 기저막, AlN 빔 어레이, 제논 에칭, MEMS, 공진 주파수, 압전 신호.

APPENDIX

Scanning Laser Doppler Vibrometer (SLDV) manual

1. System components used for measurement

(1) Micro system analyzer

- Micro system analyzer is a system component which measures the displacement and velocity of vibration using laser.

(2) Vibrometer controller

- Vibrometer controller is a system component which decodes the output signal of the displacement.

(3) Junction box

- Junction box is a central connection part between the system components and peripheral devices.

(4) Personal computer (PC)

- PC is a computer used to give the input signal and identify the measurement results.

(5) Loudspeaker

- Loudspeaker is an equipment which produce sounds.

(6) Microphone-Conditioning amplifier

- Microphone-Conditioning amplifier is an equipment to check the sound of speaker.

(7) Probe

- Probe is a component used to give and take the electric signal.

2. Cabling

(1) Measurement of displacement using acoustic stimulus

- Connect a microphone cable to the REF IN of junction box.

- Connect a speaker cable to the SIGNAL + of junction box.

- Connect a SYNC cable to the TRIG IN of junction box.

- Connect a VELO cable of junction box to the OUTPUT of controller.
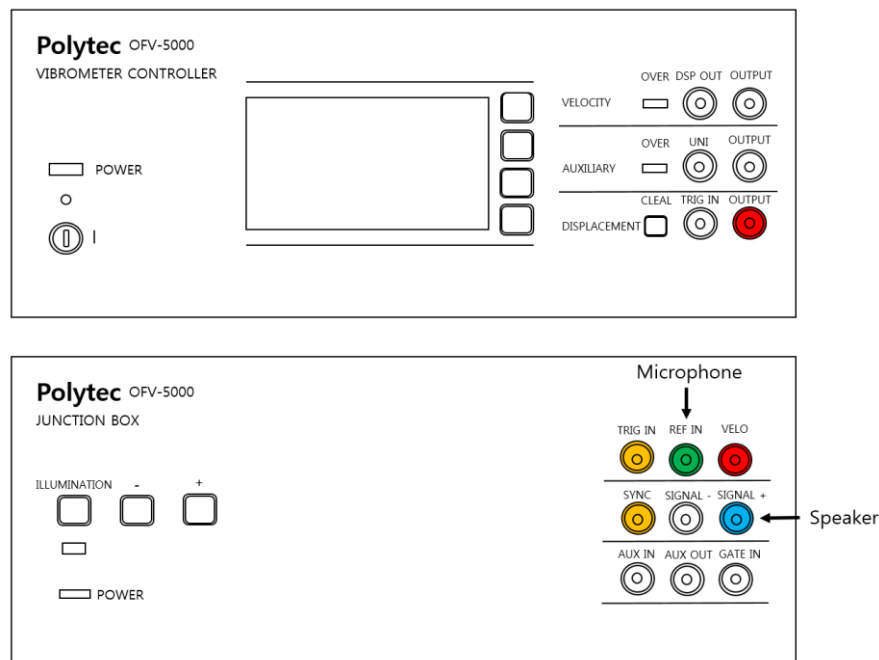
Figure 1. Front view of the controller for measurement of displacement using acoustic stimulus.

(2) Measurement of piezoelectric voltage using acoustic stimulus

- Connect a probe cable to the REF IN of junction box.

- Connect a speaker cable to the SIGNAL + of junction box.

- Connect a SYNC cable to the TRIG IN of junction box.

- Connect a VELO cable of junction box to the OUTPUT of controller.
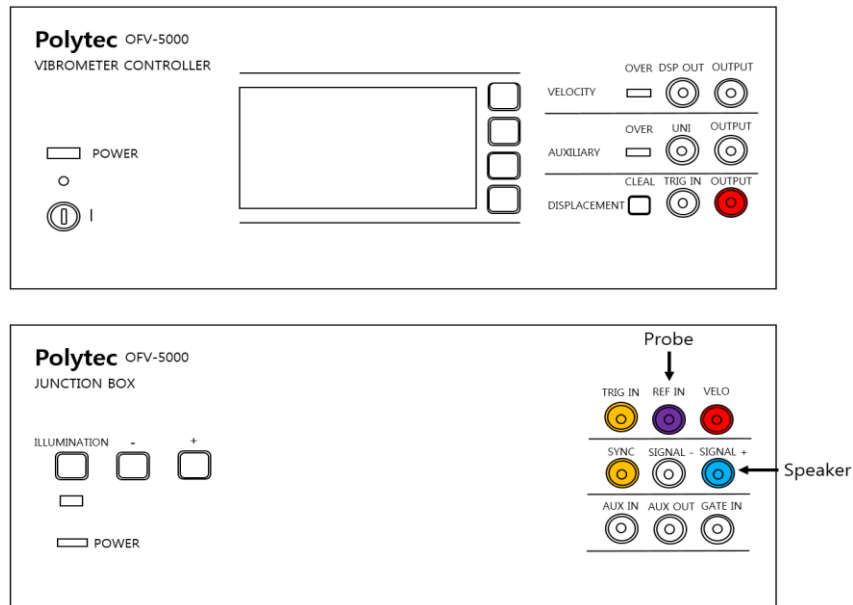
Figure 2. Front view of the controller for measurement of piezoelectric voltage using acoustic stimulus.

(3) Measurement of displacement using electric stimulus

- Connect a probe cable to the REF IN and SIGNAL + of junction box.

- Connect a SYNC cable to the TRIG IN of junction box.

- Connect a VELO cable of junction box to the OUTPUT of controller.
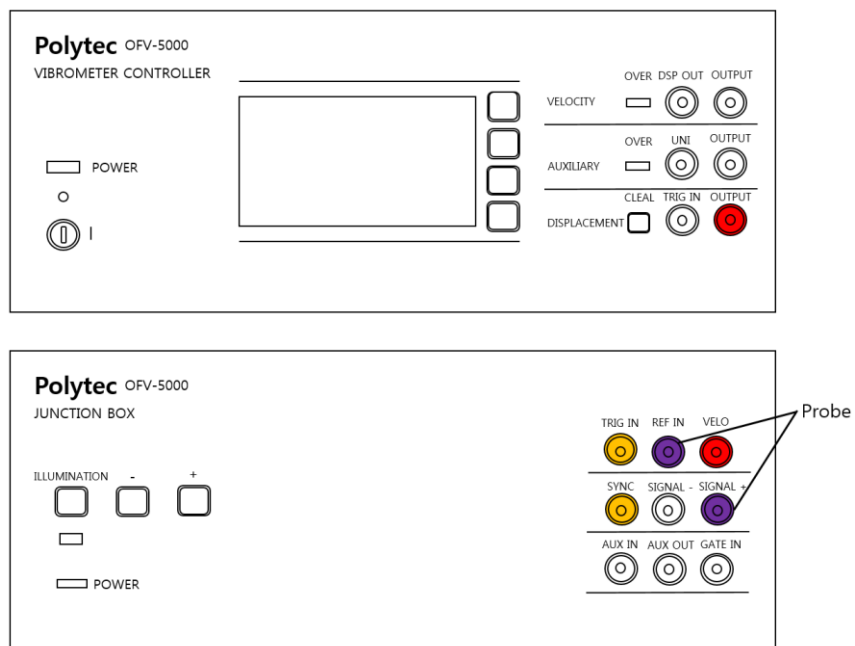
Figure 3. Front view of the controller for measurement of displacement using electric stimulus.

3. Making measurements

(1) Switching on

- Turn the controller on by setting the key switch to position l.

- Switch on the PC, start the software 'PSV Acquisition'.

- Switch on the junction box, microphone and loudspeaker.
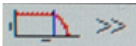
(2) Setting measurement conditions

- To set the measurement conditions, click (Acquisition Settings) icon.

- Click this word 'General', set the measurement mode, averaging list and averaging number.

- Click this word 'Channels', set the reference and output.

  *In the case of measurement of displacement using acoustic stimulus, vibrometer is set by displacement. Reference 1 is set by sound pressure.

  *In the case of measurement of piezoelectric voltage using acoustic stimulus, vibrometer is set by displacement. Reference 1 is set by voltage.

  *In the case of measurement of displacement using electric stimulus, vibrometer is set by displacement. Reference 1 is set by voltage.

- Click this word 'Filters', set the high pass filter. To set cutoff frequencies, double-click this icon.

- Click this word 'Frequency', set the frequency range of speaker and bandwidth.

- Click this word 'Vibrometer', set the velocity and displacement of controller.

- Click this word 'Generator', set the waveform.

  *Periodic chirp is a signal in which the frequency increases with time.

  *Sine is a signal which has only one frequency.

- On the small screens of four analyzer, click these icons, (Time, FFT),

  (Vib, Ref1), (Sound pressure, Voltage, Displacement).

  * In the case of measurement of displacement using acoustic stimulus,

  Screen 1: click these icon (Time), (Ref1), (Sound pressure).

  Screen 2: click these icon (FFT), (Ref1), (Sound pressure).

  Screen 3: click these icon (Time), (Vib), (Displacement).

  Screen 4: click these icon (FFT), (Vib), (Displacement).

  * In the case of piezoelectric voltage using acoustic stimulus,

  Screen 1: click these icon (Time), (Ref1), (Voltage).

  Screen 2: click these icon (FFT), (Ref1), (Voltage).

  Screen 3: click these icon (Time), (Vib), (Displacement).

  Screen 4: click these icon (FFT), (Vib), (Displacement).

  *In the case of measurement of displacement using electric stimulus,
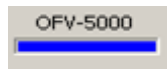
  Screen 1: click these icon (Time), (Ref1), (Voltage).

  Screen 2: click these icon (FFT), (Ref1), (Voltage).

  Screen 3: click these icon (Time), (Vib), (Displacement).

  Screen 4: click these icon (FFT), (Vib), (Displacement).

(3) Defining 2D alignment and scan points

- Place a sample on the stage of SLDV.

- From small screen of scanning, focus the lens of an optical microscope and adjust

  the brightness of the screen.

- After selecting the checkbox of joystick ☑ Joystick , take the sample's measurement location.

- To turn on the laser, select the checkbox of laser ☑ Laser .

- Click ✛ (perform 2D alignment) icon to align the laser focus.

- Try dragging the mouse to move the laser focus over the sample's measurement location. The reflectivity of laser is known from blue bar graph of optics OFV-5000 .

- Click ▦ (define scan points) icon, distribute the measuring point on the sample surface.

- After clicking a measuring point, check the reflectivity of laser.

(4) Measuring and obtaining data

- To give the input signal, Click ∿ (generator on/off) icon.

- Click ↻ (continuous) icon, start measuring the characteristics of sample.

- From small screens of four analyzer, confirm the measurement results.

- Click ✋ (stop) icon to stop sample's measurement, Click ∿ (generator on/off) icon to stop giving the input signal.

- Click certain screen of analyzer, click these words, 'File' and 'Export'.

- Click this word 'ASCⅡ', obtain the data.